Regionalizing the Sea-level Budget With Machine Learning Techniques

Carolina M.L. Camargo[1,2], Riccardo E.M. Riva[2], Tim H.J. Hermans[1,2], Eike M. Schütt[3], Marta Marcos[4], Ismael Hernandez-Carrasco[4], and Aimée B.A. Slangen[1]

[1]NIOZ Royal Netherlands Institute for Sea Research, Department of Estuarine and Delta Systems, Yerseke, The Netherlands
[2]Delft University of Technology, Department of Geoscience and Remote Sensing, Delft, The Netherlands
[3]Department of Geography, Kiel University, Kiel, Germany
[4]Mediterranean Institute for Advanced Studies (IMEDEA), Spanish National Research Council-University of Balearic Islands (CSIC-UIB), Esporles, Spain

Correspondence: Carolina Camargo, carolina.camargo@nioz.nl

Abstract. Attribution of sea-level change to its different drivers is typically done using a sea-level budget (SLB) approach. While the global mean SLB is considered closed, closing the SLB on a finer spatial scale is more complicated due to, for instance, limitations in our observational system and the spatial processes contributing to regional sea-level change. Consequently, the regional SLB has been mainly analysed on a basin-wide scale. Here we investigate the SLB at sub-basin scales,

5 using two machine learning techniques to extract domains of coherent sea-level variability: a neural network approach (Self-Organising Maps) and a network detection approach (δ-MAPS). The extracted domains provide a higher level of spatial detail than entire ocean basins and besides indicating how sea-level variability is connected among different regions. Using these domains we can close the regional SLB world-wide on different spatial scales. Steric variations dominate the temporal sea-level variability and determine a significant part of the total regional change. Sea-level change due to mass transport between ocean

10 and land has a relatively homogeneous contribution to all regions. In highly dynamic regions (e.g., Gulf Stream region) the dynamic mass redistribution is significant. Regions where the SLB cannot be closed highlight processes that are affecting sea level but are not well captured by the observations, such as the influence of western boundary currents. Hence, the use of the SLB approach in combination with machine learning techniques leads to new insights into regional sea-level variability and its drivers.

1 Introduction: The sea-level budget

Sea-level change (SLC) is one of the major challenges of the coming centuries for coastal communities worldwide (Fox-Kemper et al., 2021). Global mean SLC has been rising at a rate of 1.6 mm yr^{-1} since 1900, and 3.3 mm yr^{-1} since 1993 (Frederikse et al., 2020). However, sea level does not change uniformly: it displays strong spatial and temporal variations (Hamlington et al., 2020). Ocean dynamics, land ice mass changes and associated gravitational effects, and vertical land

20 movement are some of the processes responsible for these regional differences (e.g., Stammer et al., 2013; Slangen et al.,

2017). Understanding the regional variability of the processes driving SLC is critical for improving our understanding of its causes, constraining sea-level projections, and to better prepare for the impacts of climate change.

The attribution of SLC to its different drivers is typically done using a sea-level budget (SLB) approach. For 1993-2018, about one third of the observed rate of global mean SLC can be attributed to thermal expansion of the oceans, while the rest
25 is due to the effect of water and ice mass exchanges between land and ocean (Frederikse et al., 2020). Since the observed rate of SLC matches, within uncertainties, with the sum of the contributions of the various sources, the global mean SLB for the period 1993-2018 is considered to be closed (Cazenave et al., 2018; Frederikse et al., 2020; Chen et al., 2020; Barnoud et al., 2021). However, locally attributing the drivers of SLC for this same period still leads to large differences between the total measured change and the sum of the contributions (e.g., Slangen et al., 2014; Royston et al., 2020). This is partly due to the
30 spatial resolution of the current observational systems of the SLB components and of the processes in question, which still limits the closure of the SLB on a local spatial scale, for instance on a 1 degree resolution (Royston et al., 2020). Consequently, the regional SLB has mainly been analysed on a basin-wide scale (e.g., Purkey et al., 2014; Frederikse et al., 2018, 2020; Royston et al., 2020) and has not been closed on sub-basin scales consistently for the entire world.

The basin-scale sea-level features extracted by Thompson and Merrifield (2014) have been frequently used in regional SLB
35 studies (Purkey et al., 2014; Frederikse et al., 2018, 2020; Royston et al., 2020). Although these publications have made significant advances in understanding the regional SLC, the basin scale is still too large to really understand the causes of local variations. In this manuscript, we argue that understanding the spatial structure of contemporary SLC is a key point to move towards a higher spatial resolution budget. By identifying smaller physically coherent regions, some of the effects of small scale variability can be removed, allowing to close the budget at a sub-basin scale. Machine learning techniques, such as complex
40 and neural networks, can be used to identify such spatial structures, determining the ideal resolution and regions of common sea-level variability and change. While machine learning methods have widely been used in oceanography (e.g., Richardson et al., 2003; Liu et al., 2006; Hernández-Carrasco and Orfila, 2018; Sonnewald et al., 2019; Falasca et al., 2019, 2020), only few examples analyzing sea-surface height can be found (e.g., Liu et al., 2016; MA et al., 2016; Sonnewald et al., 2018; Novi et al., 2021). Here, we apply two unsupervised machine learning techniques –self-organising maps (SOM) and δ-MAPS– to
45 extract coherent spatial features (domains) in SLC observations.

In this study we use the extracted domains to analyse the SLB on a sub-basin scale during the satellite altimetry period (1993-2016), by using state-of-the-art estimates of SLC and its components. We limit our analysis to 2016 because of the temporal span of the hydrological models used to obtain the landwater storage contribution to SLC. Additionally, instrumental problems (e.g., in Argo salinity data and satellite drifts) have raised questions about the performance and closure of the global mean SLB
50 after 2016 (Chen et al., 2020; Barnoud et al., 2021; Cazenave and Moreira, 2022). We hypothesize that by investigating the budget in covariant and physically coherent regions, we can resolve the discrepancies (i.e., close the budget) that appear in an increased-resolution SLB (e.g., 1x1 degree).

2 Data and methods

In this section we introduce the data sets used for each of the different components of the SLB (Section 2.1). We also describe
the trend and budget analysis (Section 2.2) and introduce the machine learning techniques used to extract coherent regions
(domains) of sea-level variability and change (Section 2.3).

2.1 The components of the regional sea-level budget

For the SLB, we compare the total observed SLC η_{total} to the sum of the drivers of SLC $\eta_{drivers}$:

$$\eta_{total} = \sum \eta_{drivers}, \tag{1}$$

where η stands for the rate of SLC.

Total SLC (η_{total}) can be measured by tide gauges and satellite altimeters. Satellite altimeters measure geocentric or absolute
SLC ($\eta_{geo(sat)}$), that is, the sea surface height in relation to the reference ellipsoid (Gregory et al., 2019). On the other hand,
tide gauges measure sea surface height in reference to a terrestrial landmark ($\eta_{rel(TG)}$), registering the relative SLC. Relative
SLC is affected by vertical land motion (VLM) due to, for instance, land subsidence and tectonics (Wöppelmann and Marcos,
2015), while geocentric sea level can not differentiate if the change is either from the solid Earth or the ocean. The relationship
between geocentric and relative SLC is:

$$\eta_{total} = \eta_{geo(sat)} = \eta_{rel(TG)} + VLM. \tag{2}$$

From hereon, when we use η_{total}, we are referring to the geocentric SLC derived from satellite altimetry (Figure 1a). We use
multi-mission gridded Level-4 data from 4 distribution centers: CMEMS (CMEMS, 2022), JPL (Zlotnicki et al., 2019), SLcci
(SLcci, 2022) and CSIRO (CSIRO, 2022). All of these products use the same reference ellipsoid model (GRS80/WGS). All
data is regridded to 1x1 degree, and combined into an ensemble mean, to avoid systematic errors.

SLC expresses changes in the volume of the ocean. These can be caused by changes in the ocean density, mass or area.
Density-driven changes, known as steric sea-level changes, are caused by variations in the ocean temperature and salinity (Gill
and Niller, 1973; MacIntosh et al., 2017). All sea-level variations not driven by density changes are known as manometric SLC
(Gregory et al., 2019). Thus, Equation 1 can be rewritten to:

$$\eta_{total} = \sum \eta_{drivers} = \eta_{SSL} + \eta_{MAN}, \tag{3}$$

where η_{SSL} and η_{MAN} refer to steric and manometric SLC, respectively.

For steric SLC (η_{SSL}, Figure 1c), we use the estimates of Camargo et al. (2020), which are based on 15 different ocean
temperature and salinity data sets up to 2000m depth, using Argo floats (Roemmich and Gilson, 2009; Gaillard et al., 2016;
Li et al., 2017; Lu et al., 2019), multiple in-situ observations (Ishii and Kimoto, 2009; Guinehut et al., 2012; Cabanes et al.,
2013; Good et al., 2013; Gaillard et al., 2016; Ishii et al., 2017; Cheng et al., 2019; Szekely et al., 2019) and ocean reanalyses
(Blockley et al., 2014; Maclachlan et al., 2015; Storto and Masina, 2016; Garric and Parent, 2017; Carton et al., 2018; Zuo

et al., 2019). We complement this data with the deep ocean steric estimate of Purkey et al. (2019, updated from Purkey and Johnson (2010)).

85   Manometric SLC (η_{MAN}), also referred to as the bottom pressure term (Gregory et al., 2019), can be further divided into the (i) η_{GRD}, the Gravitational, Rotational and viscoelastic Deformation response of the Earth to water and ice mass exchanges between land and ocean, and (ii) η_{DSL}, the dynamic redistribution of ocean mass due to ocean circulation, atmosphere and ocean bottom pressure changes as a result of the steric change of the oceans (Landerer et al., 2007), following:

$$\eta_{MAN} = \eta_{GRD} + \eta_{DSL}. \tag{4}$$

90   The GRD component (η_{GRD}, Figure 1d) reflects how the mass loss of continental ice stored in glaciers and ice sheets and variations in land water storage affect sea level. The GRD effect can be split between responses due to contemporary changes, and due to the response of the Earth to the last ice age, known as Glacial Isostatic Adjustment (GIA). The integrated response of the GRD effect over the oceans, i.e. the global mean, is known as barystatic SLC (η_{BSL}, Gregory et al., 2019). For the GRD component, we use the estimates from Camargo et al. (2021, under review). These are based on a suite of different estimates of
95 land mass change, and computed solving the sea-level equation following Farrell and Clark (1976) and Slangen et al. (2014).

    The dynamic component (η_{DSL}, Figure 1e) refers to mass changes driven by bottom pressure changes, that is, the redistribution of mass that was already in the oceans. Note that, by our definition, the dynamic SLC is part of the ocean dynamic SLC (Δ_ζ, Gregory et al., 2019), which also includes the effect of local steric anomalies (η'_{SSL}). η_{DSL} is computed from the sea-surface height of ocean reanalyses (SODA (Carton et al., 2018), C-GLORS (Storto and Masina, 2016), GLORYS (Garric and Parent, 2017), FOAM-GloSea (Blockley et al., 2014; Maclachlan et al., 2015) and ORAS (Zuo et al., 2019)), by removing
100 the sea-surface height anomaly and steric estimates from it. More detail on the estimation and validation of η_{DSL} is given in Appendix A.

    Finally, equation 3 can be rewritten as:

$$\eta_{total} = \eta_{SSL} + \eta_{GRD} + \eta_{DSL}, \tag{5}$$

105 such that the total observed SLC (Figure 1a) can be compared with the sum of the components (Figure 1b). The ensemble mean of each term of Equation 5, used throughout this manuscript for the SLB analysis, is shown in Figure 1, where η_{total} is the geocentric SLC from satellite altimetry, corrected for the inverted barometer and GIA (η_{GIA}) effects; η_{SSL} is the full-depth steric SLC; η_{GRD} is the contemporary ocean mass redistribution due to the land-ocean mass exchange, already corrected for η_{GIA} effects; and η_{DSL} is the mass redistribution due to purely ocean dynamics.

110 ## 2.2   Computing Trends and Uncertainties

Our SLB is based on the comparison of sea-level trends and associated uncertainties. We assume that sea-level trends are the sum of a deterministic model (including annual and semi-annual signals) and stochastic noise (temporal uncertainty). We use the software Hector (Bos et al., 2013) to compute the trends and the associated 1-sigma uncertainty for each of the budget components. Following Bos et al. (2014); Royston et al. (2018); Camargo et al. (2020, 2021), we test 8 different noise-models
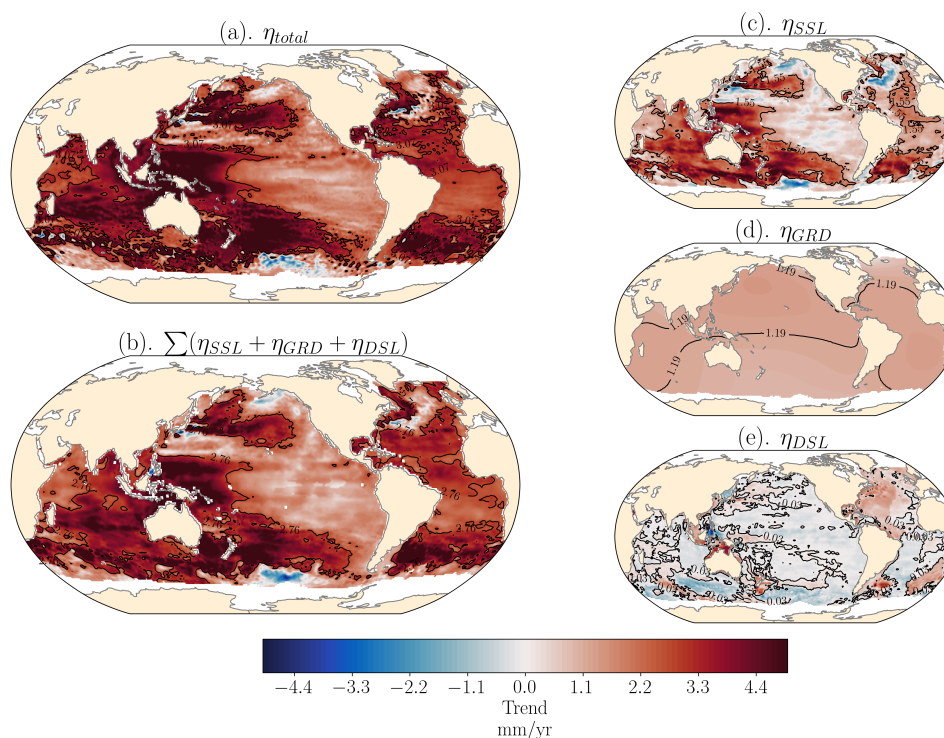
Figure 1. Regional sea-level trends for 1993-2016 (mm/yr) for (a) altimetry; (b) sum of sea-level components: (c) full-depth steric, (d) GRD effect and (e) dynamic SLC. Black contour line indicates global mean SLC.

to describe the auto-correlation between the residuals of the regression. Using the Akaike and Bayesian information criteria (Akaike, 1974; Schwarz, 1978), we select the best performing noise-model at each grid cell. More information on the noise-model analysis can be found in Camargo et al. (2020, 2021). For the GRD component, in addition to the temporal uncertainties, we also consider the spatial, structural and intrinsic uncertainties (Camargo et al., 2021).

We assume independence of the terms, and sum the trends linearly and uncertainties in quadrature. Performance of the SLB is evaluated by (i) the magnitude of the residual, (ii) the Pearson's correlation coefficient (r) between the altimetry trend and the budget components, and (iii) the normalized root mean squared error (nRMSE). nRMSE measures the distance between the true value, in this case altimetry, and the modeled value, in this case the sum of the budget components. Contrary to r, a nRMSE closer to 0 the better indicates a better performance.

2.3 Clustering Techniques

To answer our research questions, we must first identify regions with similar sea-level variability. To do so, we use two different machine learning pattern detection algorithms, one based on an neural network approach, Self-Organising Maps (SOM), and one based on a deep network detection method, δ-MAPS. The methodological differences in these two techniques leads to

different patterns of SLC in terms of geographical location, region size, and ocean coverage. Hence, by using both methods, we can (i) find prevailing sea-level modes, (ii) compare the patterns and SLB for the different methods and (iii) balance

130 out the advantages and disadvantages of using a single method. Both methods are used to reduce the dimensionality of the data, transforming high-dimensional input data into low-dimensional features (Liu et al., 2006; Falasca et al., 2020). For both clustering techniques we use satellite altimetry time-series (CMEMS, 2022), for 1993-2019, as input. Note we use a longer time-series than the ones for the budget analysis, as longer time-series can resolve better the temporal variability. However, additional tests (not shown) showed that the clustering is not strongly affected by the extra 3 years of data. We pre-process the

135 input data by removing the global mean trend, seasonality and by applying a spatial Gaussian filter of 300km width to remove small scale variability. Smaller seas, such as the Mediterranean, Baltic, Black and Caspian seas have been removed from the data prior to the clustering.

SOM (Kohonen, 1982) is a feature extraction and classification method based on an unsupervised neural network (Liu et al., 2006). We use the MatLab SOM toolbox (Vesanto et al., 2000), and follow Liu et al. (2006) and Hernández-Carrasco and

140 Orfila (2018) to choose the parameters. We apply the SOM algorithm in the time domain in order to extract the spatial patterns, herein referred to as domains, based on coherent temporal sea-level variability. Before initizaling the SOM, the 3D input data (time,lat,lon) is concatenated to 2D (time, latxlon; Richardson et al., 2003; Liu et al., 2016), and normalized to have unit variance. The network is initialized linearly, based on the first two principal components of the time series, and trained in a batch mode, that is, at each step of the training process, all input data vectors are simultaneously used to update the network. Training

145 is performed over 10 iterations, which is necessary to stabilize and converge the network, while avoiding overfitting of the SOM (Liu et al., 2006). We use the 'Epanechikov function' as a neighborhood function, which returns the most accurate SOM patterns, a hexagonal lattice, and a neighborhood radius (determining the radius of cells that are updated during the training process) of 2 cells at the beginning, decreasing linearly to 1 during the training process. We tested different SOM parameters, and verified that this combination gave the smallest quantification errors by computing the averaged Eulerian distance between

150 each data input vector and the best matching unit (BMU). SOM domains do not need to be geographically contiguous, that is, different non-connected regions can be assigned to a single domain. Initially, the strong sea-level variability of the Equatorial Pacific Ocean dominated the clustering, hindering pattern identification in the Atlantic Ocean (Supplementary Figure B6). To overcome this issue we perform the clustering analysis on the Atlantic and Indo-Pacific Ocean basins separately. We select a map size of 3x3 neurons (i.e., neural network nodes) in each basin, leading to a total of 18 domains. Using different map

155 sizes (e.g., Supplementary Figure B6) led to more "patchy" results, hence we used map size of 3x3 neurons as a compromise between the amount of detail and the interpretability of the domains.

δ-MAPS (Fountalis et al., 2018) is a complex network methodology which reduces the spatiotemporal dimensionality of a field by identifying regions (domains) with similar dynamics and their connectivity (Bracco et al., 2018; Falasca et al., 2020). Here we focus only on the domains identification (dimensionality reduction) function of the δ-MAPS method. δ-MAPS

160 domains are spatially continuous (i.e., grid cells need to be physically connected to the be clustered in the same domain) and potentially overlapping regions that have a highly correlated temporal activity (Falasca et al., 2019). Formally, each input grid cell is associated with a time series, including the K nearest neighbors, based on the haversine distance (angular distance

between two points on a sphere). The local homogeneity, defined as the average Pearson cross-correlation between a grid cell and its K-neighbors, is computed and tested against a threshold value δ. If the local homogeneity is greater than δ, with a
165 statistical significance level of 0.1, then the grid cell is considered a core, which then is expanded to identity domains (Fountalis et al., 2018; Falasca et al., 2019; Novi et al., 2021). Each domain expands to adjacent cells, as long as the local homogeneity continues to be higher than δ. To choose the optimal neighborhood size K, we follow a heuristic approach, testing K values from 4 to 25 following Falasca et al. (2019). As in δ-MAPS not every grid point needs to belong to a domain (in contrast to SOM), we then choose the K-value taking into account the amount of unclustered cells (i.e., the one with most of the ocean
170 belonging to domains). We also use the normalized mutual information (NMI) matrix (Falasca et al., 2019) to identify the K-value with high NMI for it and its neighboring K-values, meaning that the results are less sensitive to the chosen K-value. These parameters led to the use of K = 5.

3 Identifying Domains of Sea-Level Variability

Both clustering methods successfully reduce the dimensionality of the input data, despite the higher number of domains iden-
175 tified by δ-MAPS (Figure 2). SOM identified 18 coherent domains, with a domain area varying from 3.84 to 34.51 million km^2, and an average and total size of 17.61 and 316.90 million km^2. δ-MAPS identified 92 coherent domains, with a domain area varying from 0.03 to 24.15 million km^2, with average and total size of 2.53 and 242.01 million km^2. Despite the methodological differences, we find that prominent sea-level features are clustered in a similar way by SOM and δ-MAPS (Figure 2). Some of the patterns identified can be linked with known oceanic patterns, as we will discuss below. However, we note that
180 covariability does not imply a common forcing, and that some patterns may be statistically separated or grouped without a clear physical reason.

The central Pacific domain, where the variability is dominated by El Niño Southern Oscillation (ENSO) events, covers a similar region in both methods. The 'ENSO-tongue', starting from the coast of Peru and Ecuador and spreading west until the central Pacific, is identified by both methods (SOM domain 12 (pink), δ-MAPS domain 45 (light green)). The Western Tropical
185 Pacific Ocean (WTPO), influenced by ENSO and the Pacific decadal oscillation (PDO), is also identified as a single domain by both methods (SOM domain 16 (light green), δ-MAPS domain 89 (light brown)). The WTPO domains matches with the region of significant spatial correlation between steric and coastal sea-level found by (Dangendorf et al., 2021) for West Australia. In the SOM clustering, the WTPO domain incorporates the Leeuwin Current (Western Australia, Pattiaratchi and Siji, 2020) in the Indian Ocean, which is affected by waves travelling through the Tropical Australasian Seas (Feng et al., 2004). While
190 this connection is not captured by δ-MAPS, the coherence along the western coast of Australia is featured in a single domain (δ-MAPS domain 92, light pink). The Kuroshio Extension region is also identified in both methods (SOM domain 10 (brown), δ-MAPS domain 88 (brown)), reflecting how strong boundary currents influence the sea-level variability. Another example is the North Atlantic, which has similar clustering in both methods, especially in the domain south of Greenland (SOM domain 9 (light purple), δ-MAPS domain 33 (purple)), which is marked by decadal-scale SLC reflecting the strength and shape of the
195 wind-driven Subpolar Gyre and the Atlantic Meridional Overturning Circulation (Chafik et al., 2019). Within these domains,

density anomalies are known to flow southward from the Labrador Sea into the Subpolar Gyre through coastally-trapped waves (Dangendorf et al., 2021). Another region identified in both methods is the Northwestern European Shelf (SOM domain 8 (purple), δ-MAPS domain 66 (grey)), which is part of a domain that extends along the whole western European coast, continuing down to the Canary islands and well into the Atlantic. This connection could be related to the hypothesis that

200 coastally trapped waves and longshore winds cause a coherent region of sea-level variability from around the latitude of the Canary Islands up to the Norwegian Sea (Calafat et al., 2012; Chafik et al., 2019; Hughes et al., 2019; Hermans et al., 2020; Dangendorf et al., 2021). These features are in a separate δ-MAPS domain (53, green) than the Northwestern European Shelf. It is important to note that coherent features smaller than 300km are not captured in the domains because of the spatial filtering applied before the clustering analysis.

205 As SOM domains do not need to be contiguous, possible pseudo-teleconnections between different ocean regions (within the Atlantic and Indo-Pacific Ocean basins) come out of the analysis. For example, areas adjacent to the 'ENSO-tongue' domain, both north and south are clustered together in domain 18 (light blue) or in domain 15 (moss green), indicating how the ENSO signal is propagated through the Pacific, possibly through coastally trapped waves (Hughes et al., 2019) in the coastal domains (15). However, not every region classified into the same SOM domain results from a clear connection. For example, SOM

210 domain 17 (blue) groups the ocean adjacent to South Africa, the region below the Kuroshio Extension (offshore of Taiwan) and a region south of Australia and New Zealand. Another example is SOM domain 7 (salmon-pink), which implies a connection between the Atlantic Caribbean Sea and the west part of the South Atlantic Gyre (capturing parts of the Brazil Current). These regions have been classified together because they have a similar behaviour in terms of sea-level variability, but probably different forcing. Further investigation, with ocean currents, ocean-atmospheric oscillations and ocean waves are necessary to

215 explore and quantify the physical connection behind these patterns.

Unlike SOM, every δ-MAPS domain is assigned a unique number and not every pixel needs to be clustered (2a, white regions). Consequently, this method yields a larger number of domains with smaller size, while avoiding pseudo-teleconnections. The dominant sea-level modes are clear on δ-MAPS clustering, reflecting the influence, for example, of ENSO and western boundary currents on sea level. For example, the entire Caribbean (domain 87 (brown)) and Gulf of Mexico (domain 82 (red))

220 is in a single domain, highlighting the similarity in that region. The same goes for the Equatorial Atlantic (domain 86 (light purple)), the ENSO region (domains 45, 89 and 62 (light green, light brown and light brown, respectively)), and the Kuroshio current (domain 88 (brown)).

As shown in Royston et al. (2020), the components of the SLB have a similar spectral power to the total observed sea-surface height of altimetry between wavelengths of approximately 3,000 and 10,000 km. The clustering techniques applied here not

225 only reduce the dimensionality of the data, but also average out sea-level variability in regions of coherent variability, being ideal for a regional budget analysis (next section).
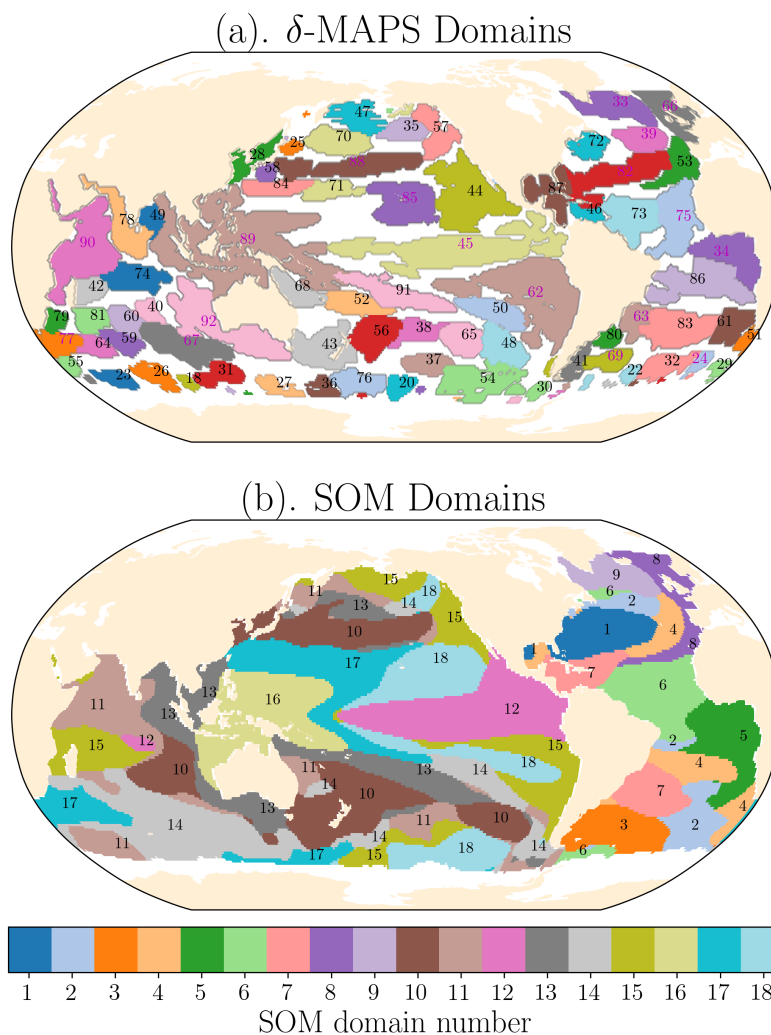
Figure 2. Domains of coherent sea-level variability. (a): δ-MAPS method (92 domains); (b): Self-Organising Maps (SOM) method (18 domains). Numbers indicate the domain code, domain names are given through the main text and in Supplementary Table B1. δ-MAPS domains with codes in magenta indicate selected domains for Figure 4. For visibility, small domains have not been labeled. Given the large number of domains, δ-MAPS has a repeating color pallet, but since δ-MAPS domains need to be continuous, repeated colors do not indicate the same domain. White regions in δ-MAPS indicate incoherent regions, which were not incorporated in any domain.

4 The Regional Sea-Level Budget on Different Spatial Scales

4.1 Sea-Level Budget Closure

We investigate the SLB on different spatial scales, from a finer (1x1 degree) to coarser scale (δ-MAPS and SOM domains; Figure 3). The residuals (i.e., the difference between the total SLC and the sum of the components) decrease towards a coarser spatial scale: for 1 degree, they range from -8.0 to 20.0 mm yr^{-1}, while for δ-MAPS they range from -1.5 to 3.7 mm yr^{-1}, and for SOM from -0.3 to 0.5 mm yr^{-1}. This shows an improvement of the budget closure (i.e., total and sum of components agree within uncertainties) by using the pattern detection algorithms: the budget closes in all 18 SOM domains (100% of SOM ocean area), in 77 out of 92 of the δ-MAPS domains (96% of δ-MAPS ocean area (232 million km^2)) and in 85% of the grid cells in the 1 degree budget (88% of the ocean area) (Figure 3). The good closure in the 1 degree budget is likely an artefact of the large uncertainties of the observations, which on a local scale can be up to 18 mm yr^{-1} (see Supplementary Figure B2). This is in line with Royston et al. (2020), who found that local biases of steric estimates together with the resolution limitation of GRACE observations over the oceans hinder the budget closure at 1 degree resolution. When the regional domains based on SOM and δ-MAPS are considered, the uncertainties show a sixfold reduction compared to the 1 degree resolution, reaching up to 3 mm yr^{-1} and an average value of 1.5 mm yr^{-1} (Supplementary Figure B2), while the budget still closes.

Consequently, there is a better match between the total observed rate of SLC with the sum of the components for the clustered regions (scatter points in Figure 3, right column), with a reduction in the spread of the scatter points and moving closer to the 1:1 line (black dashed line) for the coarser resolutions. The dashed pink lines in Figure 3 indicate the half-width of the 95% confidence interval of the uncertainty of the residuals, showing a slightly larger width for 1 degree, and a smaller one for SOM and δ-MAPS. Even when the components uncertainties (grey error bars) are considered, the scattered values are mostly within the width of the 95% confidence interval for the SOM domains, confirming the improvement of the budget for this case. There is a strong linear correlation between the total and the sum of the drivers, with Pearson's r varying from 0.74 for the 1 degree budget to 0.80 for δ-MAPS and 0.98 for SOM. The RMSE also decreases for the coarser scales, from 0.95 mm/yr for the 1x1 budget to 0.30 mm yr^{-1} for the SOM domains.

The altimetry trends are generally larger than the sum of the SLC drivers, as indicated by the positive residuals and scatter points above the 1:1 line on Figure 3. This is true for more than half of the δ-MAPS domains and for all SOM domains except one: SOM domain 9 (South of Greenland) is marked by a negative residual, that is, the sum of the drivers is larger than the observed altimetry trend. Several δ-MAPS domains, such as Southwest of Australia (domains 92 and 67), Southeast Pacific (domains 37 and 54), Gulf Current (domain 82) and Brazil-Malvinas confluence zone (domains 80 and 69), also have a negative residual. This might indicate a larger temporal variability or regime shifts in this region, or might be due to the ocean dynamics contribution, such as the effect of the Subpolar Gyre around the south of Greenland (Chafik et al., 2019), as we will see in the next section (Section 4.2).
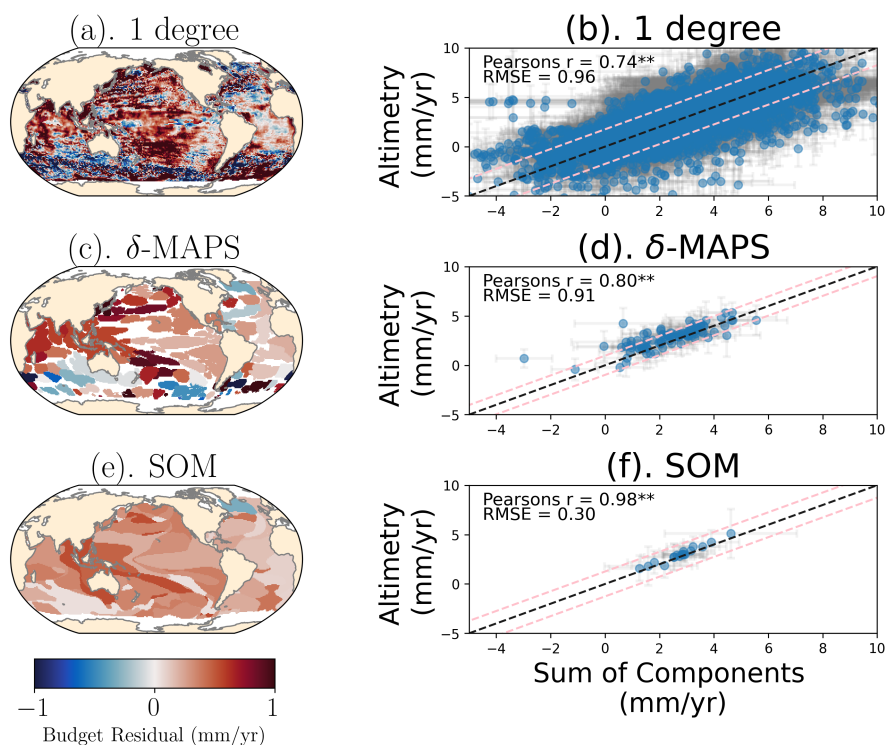
Figure 3. Sea-level budget residuals (maps(a,c,e)) and comparison between total sea-level change (y-axis) and sum of components (x-axis) (scatter plots (b,d,f)) for 1 degree (a,b), δ-MAPS domains (c,d) and SOM domains (e,f). Gray lines indicate the uncertainties of the components. In the scatter plots every point indicates one region (grid in case of 1degree), pink dashed lines indicate the half-width of the 95% confidence interval of the residuals uncertainty, grey error bars indicate the component uncertainty. ** indicates that coefficient is statistically significant (p-value <0.01).

4.2 Explaining the Sea-Level Budget Contributions

In this section, we investigate which components dominate the trend and temporal variability in each of the different domains. For comparison and discussion purposes, we choose 18 δ-MAPS domains (magenta numbers, Figure 2b) located close to the 18 SOM domains. Trends for all δ-MAPS domains are available online as an interactive map (see caption Figure 4).

As shown previously, we find a good match of total observed SLC and the sum of components (Figure 4a,b, green stars and purple triangles, respectively) for all SOM and δ-MAPS domains. The largest budget uncertainties, considering both altimetry and the sum of components, is seen in the WTPO domain (SOM 16, δ-MAPS 89). These uncertainties may be related to: (i) poor performance of standard altimetry products in these shallow regions; (ii) poor Argo float coverage in the region (Kleinherenbrink et al., 2017), influencing both the steric and dynamic components; and (iii) large internal variability due to ENSO events in this region, which may contribute to large temporal uncertainties in the steric and altimetry components (Kleinherenbrink et al., 2017; Wagner and Böning, 2021). This region is also within the Indian-south Pacific basin (Thompson

and Merrifield, 2014), which was the only basin in which the regional budget from 2005-2015 could not be closed (Royston
270 et al., 2020).

The GRD component (Figure 4, blue) has a relatively comparable contribution to all regions, contributing about $1.5\,\mathrm{mm\,yr^{-1}}$ of sea-level rise. The dynamic and steric components, however, show a strong regionally varying contribution (Figure 4, red and yellow, respectively). For example, for SOM (δ-MAPS) domains 10 (88), 13 (92), 14 (67) and 16 (89), more than 50% of the total trend is due to steric variations. On the other hand, for SOM domains 1 and 18 and δ-MAPS domains 39, 45 and 275 62, the steric trend explains less than 20%. The dynamic component shows a small contribution for most of SOM domains, and in some domains even a negative trend (e.g., SOM domain 11, 12 and 14). An exception is the Gulf Stream domain (SOM 1, δ-MAPS 82), where almost half of the total trend is explained by the dynamic component. This dominance of the dynamic component reflects the influence of the strong western boundary current on sea level in this region. The south of Greenland domain (SOM 9, δ-MAPS 12) also includes a relatively large dynamic contribution, with a trend of $0.49 \pm 0.21\,\mathrm{mm\,yr^{-1}}$, 280 reflecting the influence of the Subpolar Gyre in this region. The dynamic component also has a significant contribution to other δ-MAPS domains, such as domains 24, 69, 39, 66 and 67. Domain 67, located southwest of Australia, shows a large negative dynamic trend, which can be related to the influence of the West Australian Current.

Regarding the temporal evolution (Figure 4c,d and Supplementary Figure B4), both SOM and δ-MAPS time series show a similar behaviour. The steric component dominates the temporal sea-level variability, with a good match to the altimetry. The 285 time series of 'ENSO-tongue' domain (SOM 12 and δ-MAPS 45, Figure 4d) shows the clear response of sea level to ENSO, with peaks coinciding with strong ENSO events, such as the El Niño of 1997 and 2015. The prominent contribution of the dynamic component to the total trend in the Gulf Stream domain (SOM 1 and δ-MAPS 82) is not reflected in the time series (Figure 4c). Hence, while the dynamic component has a significant impact on the overall change, it does not contribute to the seasonal to interannual sea-level variability. This is true for all other domains (Supplementary Figure B4), except for SOM 290 (δ-MAPS) domain 2 (24) and 18 (85), where we find a better match between the dynamic and altimetry time series.

4.3 Sea-Level Budget Sensitivity

Here, we investigate the sensitivity of the budget considering (i) the components included in the budget, (ii) the size of the domains and the clustering method, and (iii) the data sets used for each component.

To illustrate the performance of the budget considering the domains used and the components included in the budget, we 295 show how the Pearson's correlation coefficient (r) and the normalized root mean squared error (nRMSE) change when these factors vary (Figure 5). This figure firstly shows that the budget closure improves when more components are included in the budget. While we get a poorer performance when only considering the dynamic or the GRD component, the budget with only steric already performs relatively well. Possibly, by removing the global mean steric signal of the steric component, the local steric anomaly and the dynamic components should have a similar performance on the budget. The budget performance is 300 enhanced by the addition of the dynamic and GRD components, shown by the narrowing of the box-and-whiskers plot.

The figure also shows an improvement of the budget closure for δ-MAPS and SOM domains, in relation to the 1 degree resolution, regardless of the budget combination. There are two possible reasons why a coarser spatial resolution leads to
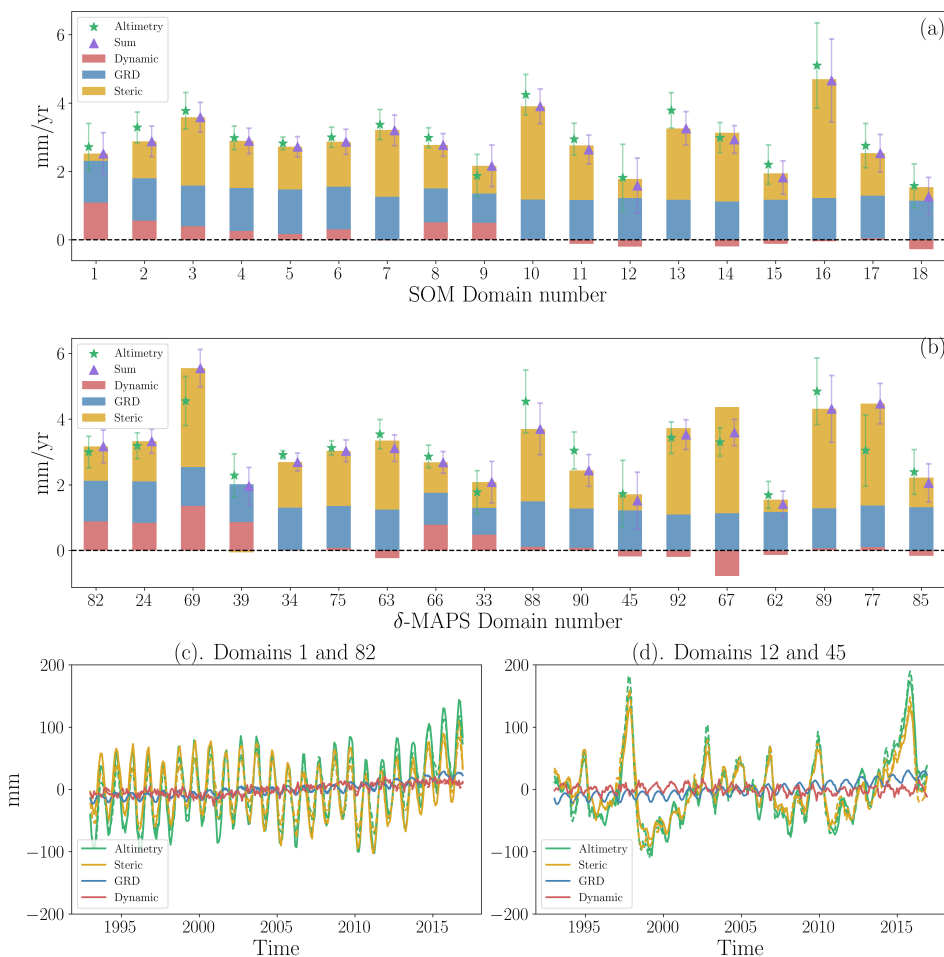
Figure 4. Sea-level budget trends (mm/yr) for (a) δ-MAPS domains and (b) SOM, and (c,d) time series for two example domains. Location of each domain is shown in Figure 2 (domain numbers in magenta for δ-MAPS). For comparison δ-MAPS domains are matched to the SOM domains, for example SOM domain 12 to δ-MAPS domain 45. Bar plot for all other δ-MAPS domains can be found in Supplementary Figure B3. For time series, solid and dashed lines indicate SOM and δ-MAPS time series, respectively. Time series for all SOM domains and for the 18 δ-MAPS domains in (b) are shown in Supplementary Figure B4. An interactive budget map is available at https://carocamargo.github.io/portfolio/portfolio-1/ for both SOM and δ-MAPS.

decreasing uncertainties and a better budget closure: (i) the spatial scale of the process itself, as changes in long-term sea
level typically occur on a coarser resolution than 1 degree; and/or (ii) there is a mismatch in the exact location between
305   the sum of the components and altimetry observations on a finer spatial scale, resulting from the limited resolution of the
observations, compared to a coarser scale when such mismatches are partially averaged out. Simply upscaling the resolution
of the observations – i.e, considering 2x2 or 5x5 degrees blocks – does not have the same effect on budget performance as the
domains derived by machine learning (Supplementary Figure B5): there is demonstrated added value of considering regions
that are physically coherent, rather than artificial blocks, for the budget analysis. That is, spatially averaging over areas of
310   similar variability reduces the unexplained variance of the observations.
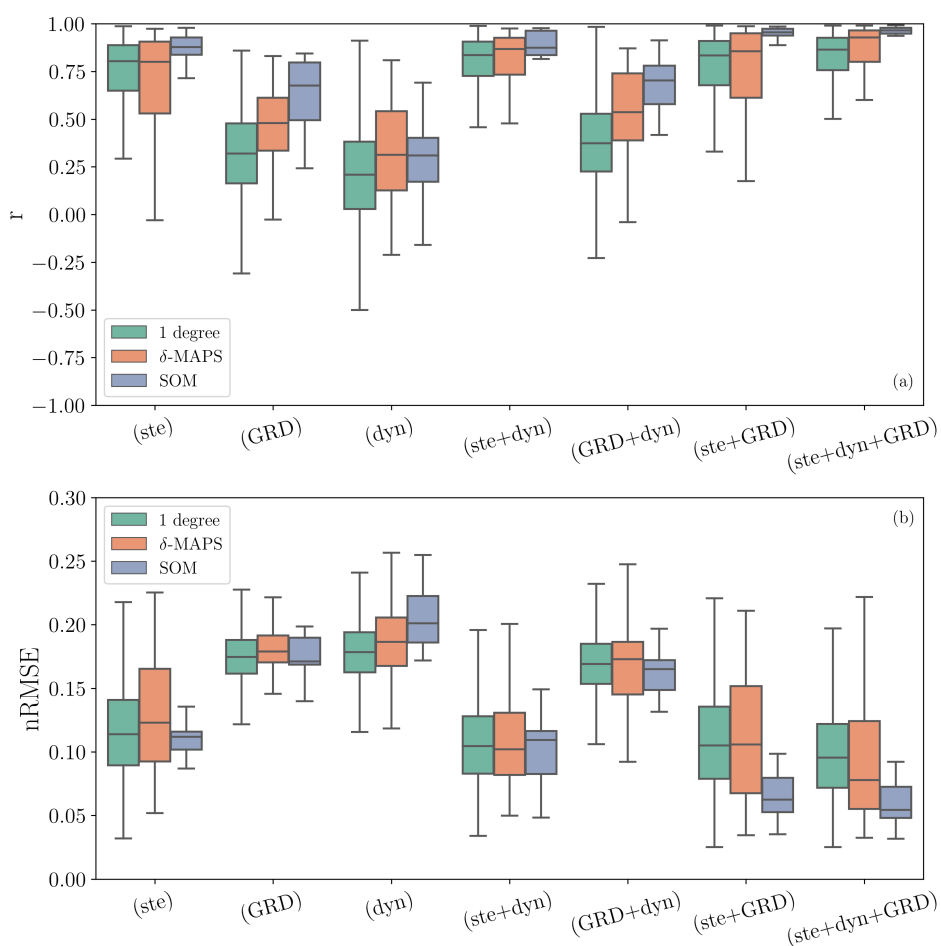
Figure 5. The effect on budget closure for different component combinations and spatial resolutions. (a) Pearson's correlation coefficient
(r) and (b) normalized root mean squared error (nRMSE), in mm yr^{-1}, between total sea-level (altimetry) and the different components
included in the budget (x-axis), for the different spatial resolutions (1 degree in green, δ-MAPS in red and SOM in blue).

When it comes to the data sets of the different SLC drivers, SLB studies often use the ensemble mean of several data sets for each component (e.g., Cazenave et al., 2018), or they compute a range of budget combinations, by varying the data set for each component, to find the combination that returns the best budget closure (e.g., Gregory et al., 2013). The latter approach can result in a budget closure for the wrong reasons (Royston et al., 2020). On the other hand, while the ensemble mean approach
315 may reduce the systematic biases of using individual data sets (Storto et al., 2017), it may also hinder the real variability of the process being analysed (Rougier, 2016). Alternatively, the budget can be analysed with the data sets closest to the ensemble means, according to the RMSE analysis, which retains the true variability of an individual data set (Rougier, 2016; Royston et al., 2020).

All the results presented so far were computed using the ensemble means for each component, considering 15 steric, 5
320 dynamic, 4 barystatic and 4 altimetry data sets. Considering all single data sets plus the ensemble of each component we can obtain 2400 possible budget combinations (16x6x5x5). To illustrate the dependence of the budget closure on the data set used, we now also discuss the residuals of each SOM domain considering all 2400 possible data set combinations (Figure 6). The residual value shows a large spread for the different budget combinations, ranging from about -2 to 2 mm yr^{-1}, and 34% of the combinations would result in non-closure of the budget (i.e., the sum of the components does not match with the altimetry
325 values, indicated in red).

The residuals of the ensemble combinations (used throughout this study, and indicated by the blue filled squares in Figure 6) are comparable with the residuals of the combinations using the data sets with the smallest RMSE to the ensemble mean (indicated with purple filled triangles in Figure 6). With the exception of the domains 14 and 16, we see that the ensemble and the RMSE combination have a similar residual value. This indicates that the closure of the budget is not an artefact of the data
330 set choice.

5 Discussion & Conclusions

SLB assessments are important tools for understanding the processes driving SLC, for detecting temporal changes in sea-level and its components, for identifying missing contributions to the budget, and for validating and constraining climate models used in sea-level projections (Cazenave and Moreira, 2022). In particular, understanding the processes on a finer spatial scale
335 is essential for local sea-level projections and coastal management planning. In this study, we investigated the regional SLB for 1993-2016 on a global scale.

Regional SLB closure tends to be difficult due to the complex physical processes acting on different spatial scales. To overcome this spatial resolution issue, we applied a neural network approach, SOM, and a deep-network detection method, δ-MAPS, to identify domains of coherent sea-level variability (Figure 2). The identified patterns reflect, among others, the in-
340 fluence of natural internal climate modes (Han et al., 2017), such as ENSO, PDO and NAO. This indicates the potential of using machine learning and pattern detection algorithms, such as SOM and δ-MAPS, to isolate the effects of natural climate modes from anthropogenic forcing on SLC. The domains also suggest how sea-level variability may be transferred between ocean regions. For example, the Northwestern European Shelf SOM domain extends south down to the Strait of Gilbratar, possibly
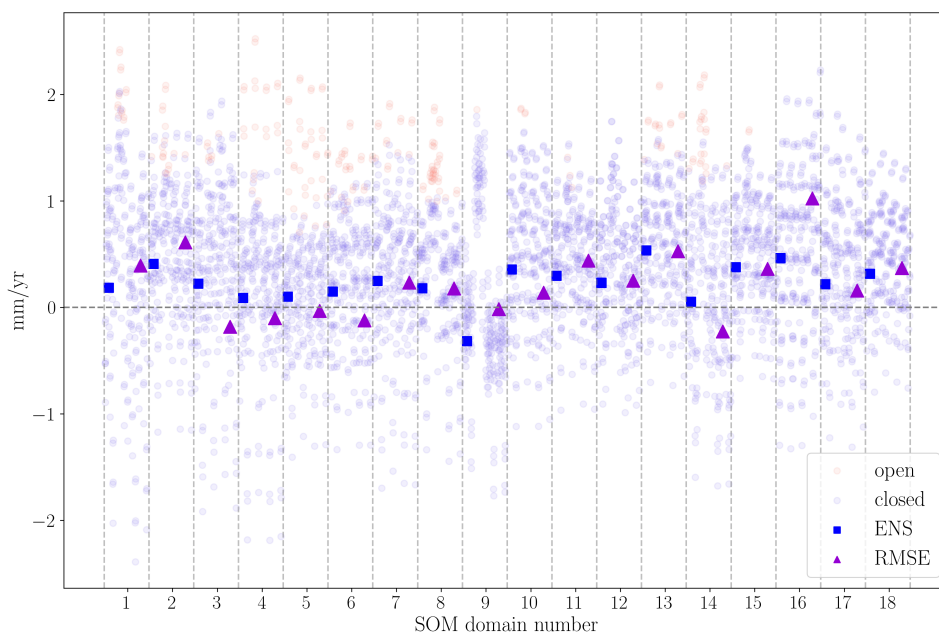
Figure 6. Budget residuals (mm/yr) for all possible data sets combinations for every SOM domain (separated by vertical dashed lines). The ensemble mean combination (used for the main analysis) is indicated with squares. The RMSE combination, that is, the budget combination using for each component the individual data set with smallest RMSE in relation to the ensemble mean, is indicated with triangles.

reflecting how coastally-trapped waves propagate sea-level variability into the North Sea (Hughes et al., 2019; Hermans et al.,

345   2020; Dangendorf et al., 2021). Additionally, highly energetic ocean regions, such as the Kuroshio current, the Gulf Stream and the Malvinas confluence zone, are also extracted as single features, matching the spectrum of sea-level variability in those zones (Hughes and Williams, 2010).

Compared with the basin regions of Thompson and Merrifield (2014), we have identified more and smaller domains, especially in the Southern hemisphere. This means our domains can provide an additional level of spatial detail compared to ocean

350   basins, while remaining large enough to provide a consistently closing regional SLB. Using the domains identified with SOM and δ-MAPS, we presented a regional SLB assessment on an average scale of about $30 \cdot 10^6 km^2$. The performance of the budget improves from finer (1 degree resolution) to coarser scale (SOM domains), with a residual spread of 0.8 mm yr^{-1} for SOM compared to 28.0 mm yr^{-1} for 1-degree resolution. We also showed that the budget closes better when all components (steric, dynamic and GRD) are included, highlighting the importance of including the deep steric and dynamic contributions

355   to regional SLC. Despite the large uncertainties at a regional scale (compared to the global mean) (Royston et al., 2020), we were able to identify dominant drivers in most domains. Regions where the SLB cannot be closed highlight processes that are affecting sea level but are not well captured by the observations, such as the influence of western boundary currents.

The GRD component has a relatively homogeneous contribution, independent of the domain, in agreement with Frederikse et al. (2020). The steric contribution dominates the seasonal and interannual variability, and results in the prevailing sea-level

360 trend in most domains, especially for domains in the southern hemisphere and equatorial regions. The dynamic component is important in some regions, particularly in the Gulf Stream domain. The domains where the dynamic component plays an important role coincide with the coastal polygons of Rietbroek et al. (2016) where a large part of the budget could not be explained solely by the sum of steric and land-ocean mass exchange. Hence, our analysis sheds light on the unexplained variance of previous SLB studies.

365 Here we showed that pattern detection techniques based on machine learning, such as SOM and δ-MAPS, are powerful approaches for identifying and understanding features of global sea-level change and variability. The domains identified in this research highlight that different ocean regions are interconnected, revealing how large-scale circulation controls regional sea level. These domains are not only a good starting point for a regional SLB analysis, but also have the potential to separate natural and anthropogenic forcings of SLC in a detection and attribution approach, building on previous work (e.g., Marcos

370 and Amores, 2014; Slangen et al., 2014, 2016). Future work may include multiple linear regressions with climate modes to explore this potential. Additionally, these domains can also be used for coastal sea-level reconstructions (e.g., as Dangendorf et al. (2021)) and for pattern scaling in sea-level projections (Bilbao et al., 2015).

Code and data availability. Sea-level trends and scripts used for the budget analysis are available at 10.5281/zenodo.7007331 (reserved link to be published after manuscript acceptance) and https://github.com/carocamargo/SLB

375 **Appendix A: Dynamic Sea-level Change Estimation and Validation**

The dynamic redistribution of mass due to ocean circulation, atmosphere and ocean bottom pressure changes as a result of the steric change of the oceans is known as dynamic sea-level change (η_{DSL} Landerer et al., 2007). η_{DSL} refers to mass changes driven by bottom pressure changes, that is, the redistribution of mass that was already in the oceans. Note that, by our definition, the dynamic SLC is part of the ocean dynamic SLC (Δ_ζ, Gregory et al., 2019), which also includes the effect of

380 local steric anomalies (η'_{SSL}). When the ocean dynamic component ($\Delta\zeta$) is considered together with the global mean steric SLC ($\overline{\eta_{SSL}}$), then it is known as sterodynamic SLC (η_{SDSL}, Gregory et al., 2019; Dangendorf et al., 2021; Wang et al., 2021). By decomposing the steric component in a global mean (denoted with the overline bar) and local anomaly component (denoted by the prime symbol), we can write the sterodynamic equation as:

$$\eta_{SDSL} = \Delta\zeta + \overline{\eta_{SSL}} = \eta_{DSL} + \eta'_{SSL} + \overline{\eta_{SSL}} \tag{A1}$$

385 To obtain Δ_ζ, we use the sea-surface height of 5 ocean reanalysis data sets (SODA (Carton et al., 2018), C-GLORS (Storto and Masina, 2016), GLORYS (Garric and Parent, 2017), FOAM-GloSea (Blockley et al., 2014; Maclachlan et al., 2015) and ORAS (Zuo et al., 2019)). As ocean reanalyses are mass conserving (Griffies and Greatbatch, 2012), the sea-surface height of a reanalysis does not include the GRD component, but it does include the steric effect. We acknowledge that this method might introduce some circularity to the budget analysis: the reanalysis, used to obtain η_{DSL}, assimilate satellite sea-surface height,

390 and in the budget analysis we compare this estimate with satellite sea-surface height (η_{total}). Following Wang et al. (2021) we

compute ocean dynamic SLC by removing the time-varying global mean from the reanalysis' sea surface height:

$$\Delta\zeta = \eta_{rea} - \overline{\eta_{rea}}. \tag{A2}$$

Since we are interested purely in the dynamic part of Δ_ζ, that is, the dynamic SLC (η_{DSL}), we must remove the steric local anomaly (η'_{SSL}) as:

395 $$\eta_{DSL} = \Delta\zeta - \eta'_{SSL} = \Delta\zeta - (\eta_{SSL} - \overline{\eta_{SSL}}), \tag{A3}$$

where the steric estimate has been computed with the ocean temperature and salinity of the respective reanalysis. We then compute the ensemble mean of the 5 dynamic estimates.

To validate our estimate of η_{DSL}, we compare it with η_{DSL} estimated from Gravity Recovery and Climate Experiment Satellite (GRACE, Tapley et al., 2004). GRACE measures total mass changes, that can be used to derive estimates of mano-
400 metric sea-level change over the oceans (Chambers et al., 2004; Royston et al., 2020). We use GRACE mass concentrations (mascons) products over the oceans from two different processing centres: RL06 from the Center for Spatial Research (CSR, Save et al., 2016; Save, 2020) and RL06 v02 from the Jet Propulsion Laboratory (JPL, Watkins et al., 2015; Wiese et al., 2019). In order to obtain the η_{DSL}, we then remove the GRD patterns obtained for the same data sets by Camargo et al. (2021). Note that we use GRACE dynamic SLC for validation purposes, but not in our budget analysis, as this data set only starts in 2002.
405 Qualitatively, η_{DSL} obtained from GRACE (Figure A1a) and from ocean reanalysis (Figure A1b) agree on large scale patterns and magnitude of dynamic changes, despite local differences (Figure A1c). The main differences are in the region surrounding Indonesia an Japan, related to the signature of the 2004 Sumatra (Indonesia) and 2011 Tokohu (Japan) mega-thrust earthquakes (Chen et al., 2007; Ghobadi-Far et al., 2020) on GRACE observations. To a lesser extent, we also see the effect of the 2010 Maule (Chile) earthquake and tsunami (Ghobadi-Far et al., 2020). Another strong divergence is seen in the
410 South Atlantic, where the positive trends of GRACE are not represented in the reanalysis, possibly suggesting that a source of dynamic SLC is not well parameterized in the reanalysis.

Appendix B: Supplementary Figures and Tables
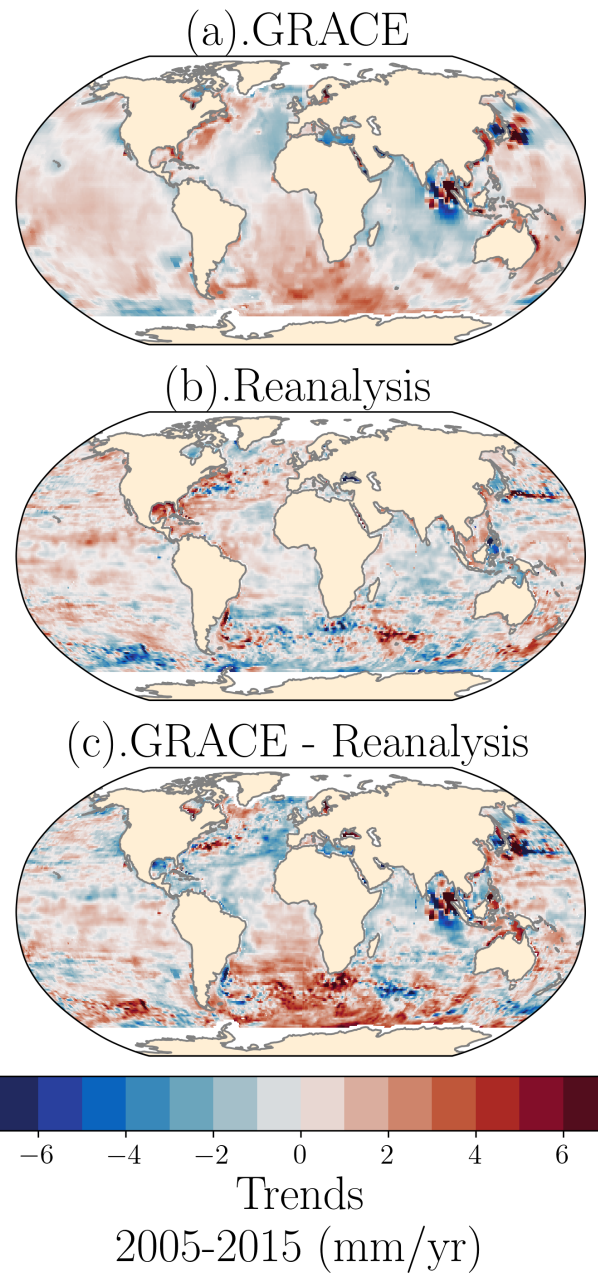
Figure A1. Dynamic SLC (η_{DSL}) estimated from (a) GRACE (average of JPL and CSR mascons), (b) ensemble of ocean reanalysis, (c) difference between GRACE and reanalysis.
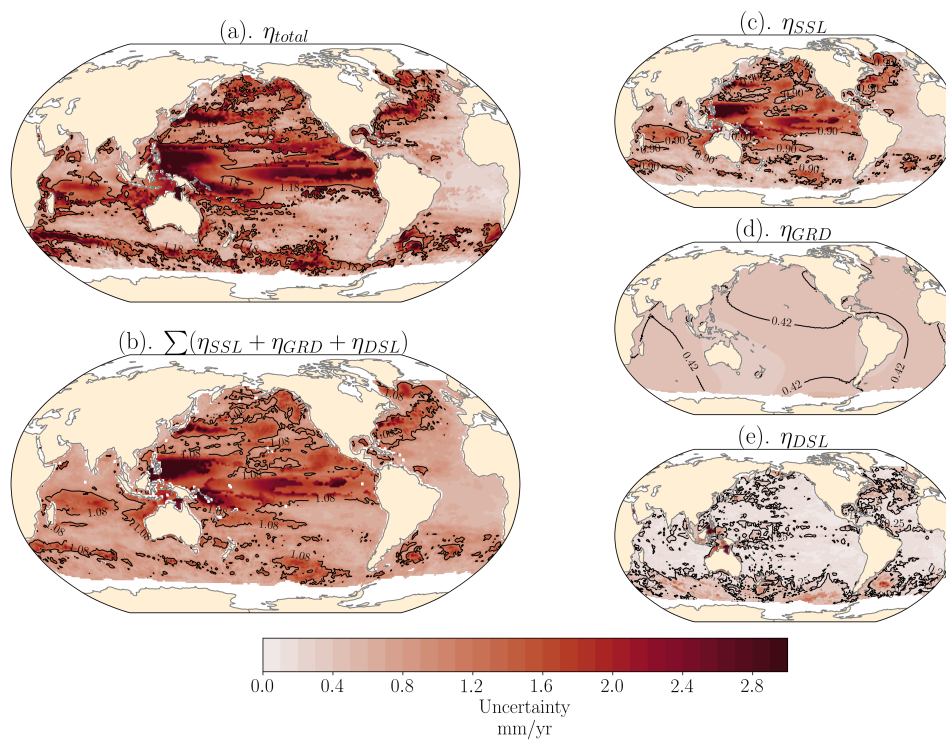
Figure B1. Uncertainties of the regional sea-level trends (Figure 1) for 1993-2016 (mm/yr) for (a) altimetry; (b) sum of sea-level components: (c) full-depth steric, (d) GRD effect and (f) dynamic SLC. Black contour line indicates global mean SLC.
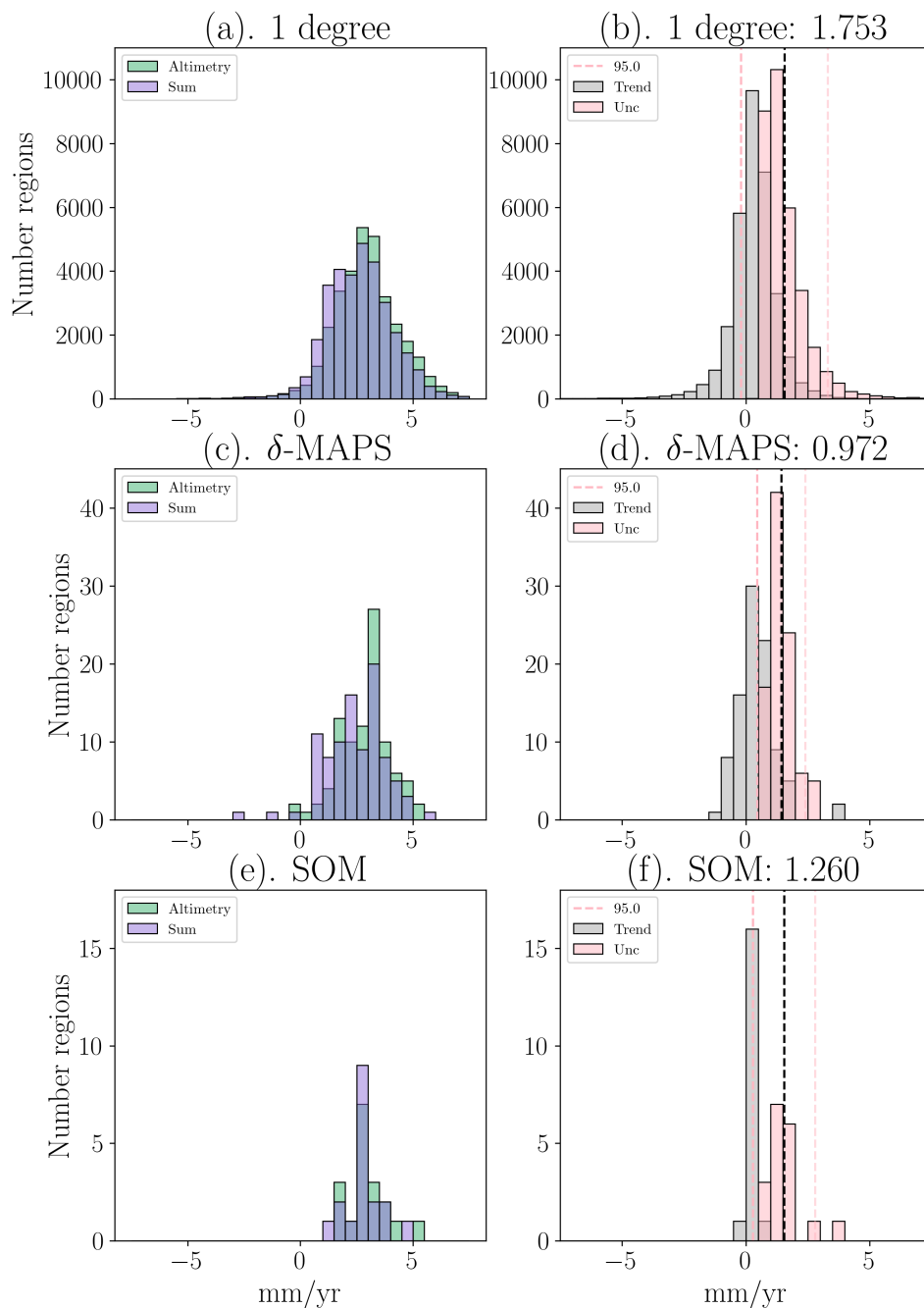
Figure B2. Distribution histograms of the altimetry (left column, green blocks), sum of the components (left column, purple blocks) and residuals trend (right column, gray) and uncertainty (right columns, pink), for the 1x1 degree budget (top row), δ-MAPS domains (middle) and SOM domains (bottom). The dashed pink lines indicate the 95% confidence interval of the residuals uncertainty, with the interval width reported in the subplots titles, and was used as a reference for the residuals scatters in Figure 3

Table B1. Names of SOM and δ-MAPS domains

SOM	δ-MAPS	Domain name
1	82	Gulf Stream
2	24	Southeast Atlantic
3	69	Malvinas Current
4	39	Central North Atlantic Gyre
5	34	East Africa Atlantic coast
6	75	East Equatorial Atlantic
7	63	Brazil Current
8	66	Northwest European Shelf
9	33	South of Greenland
10	88	Kuroshio Extension
11	90	Northwest Indian Ocean
12	45	ENSO-tongue'
13	92	Southwest Autralia, Freemantle region
14	67	Southweast Indian Ocean
15	62	Southwest Tropical Atlantic Ocean
16	89	West Tropical Pacific Ocean, Australiasian Seas
17	77	Agulhas Current
18	85	Central North Pacific Ocean
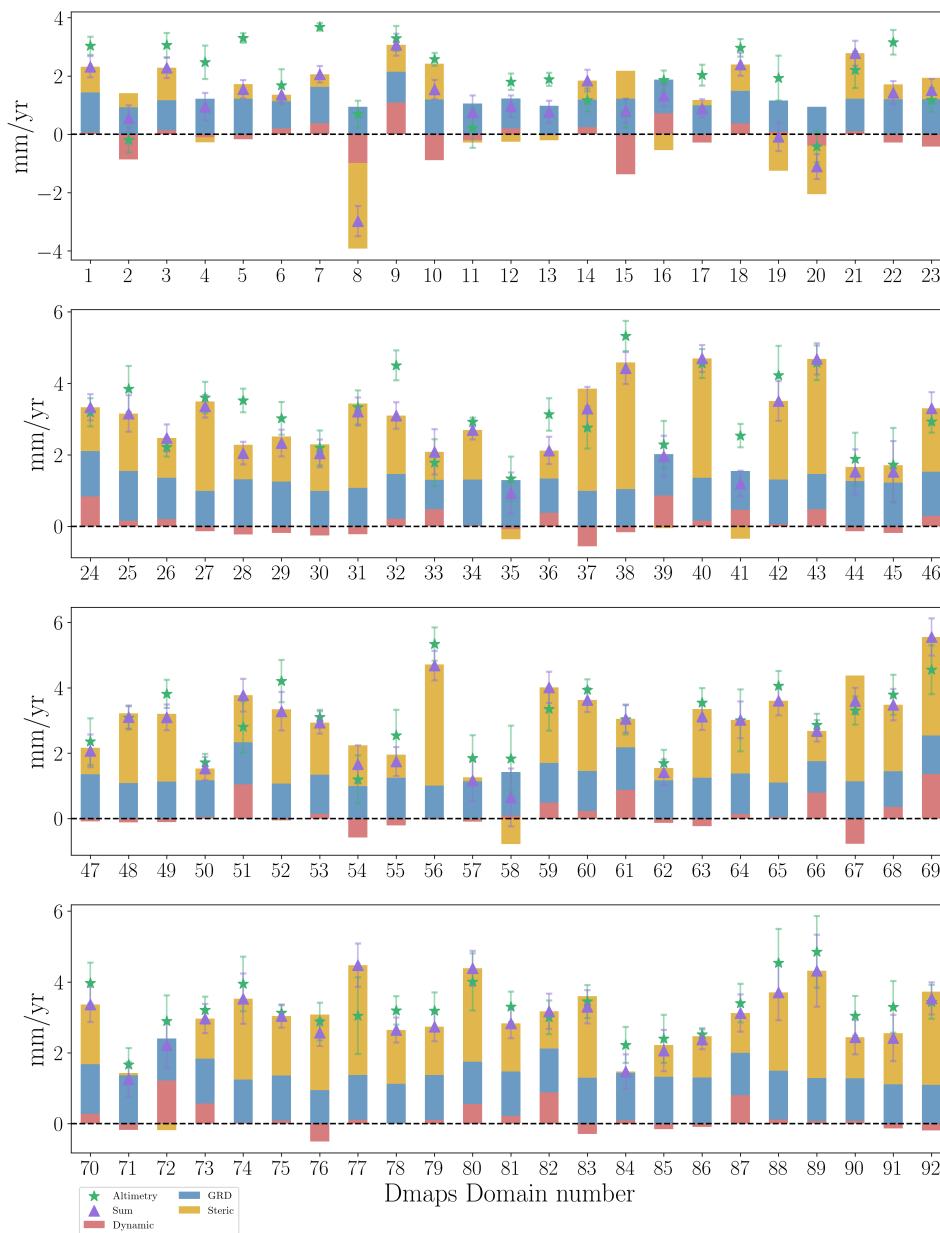
Figure B3. Extension of Figure 4, showing the trend contribution for each δ-MAPS domains. An interactive budget map is available at https://carocamargo.github.io/portfolio/portfolio-1/
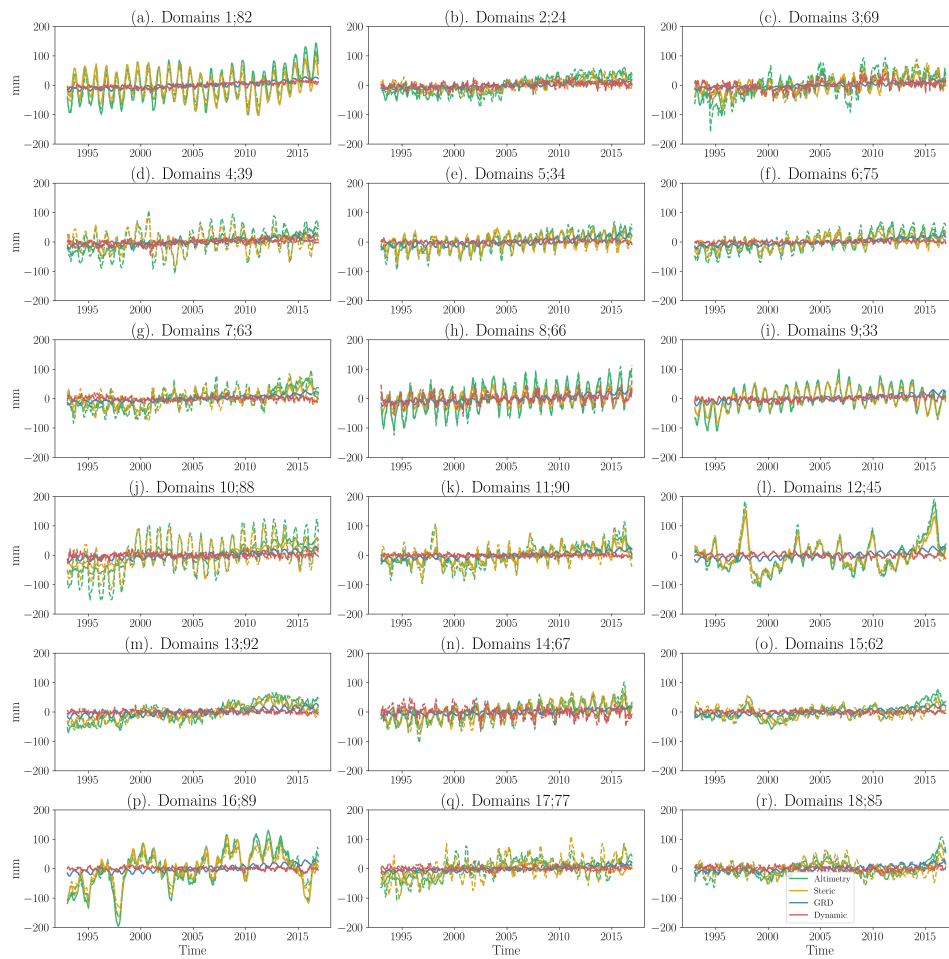
Figure B4. Extension of Figure 4, showing the time series for each of the SOM domains and corresponding δ-MAPS domains.
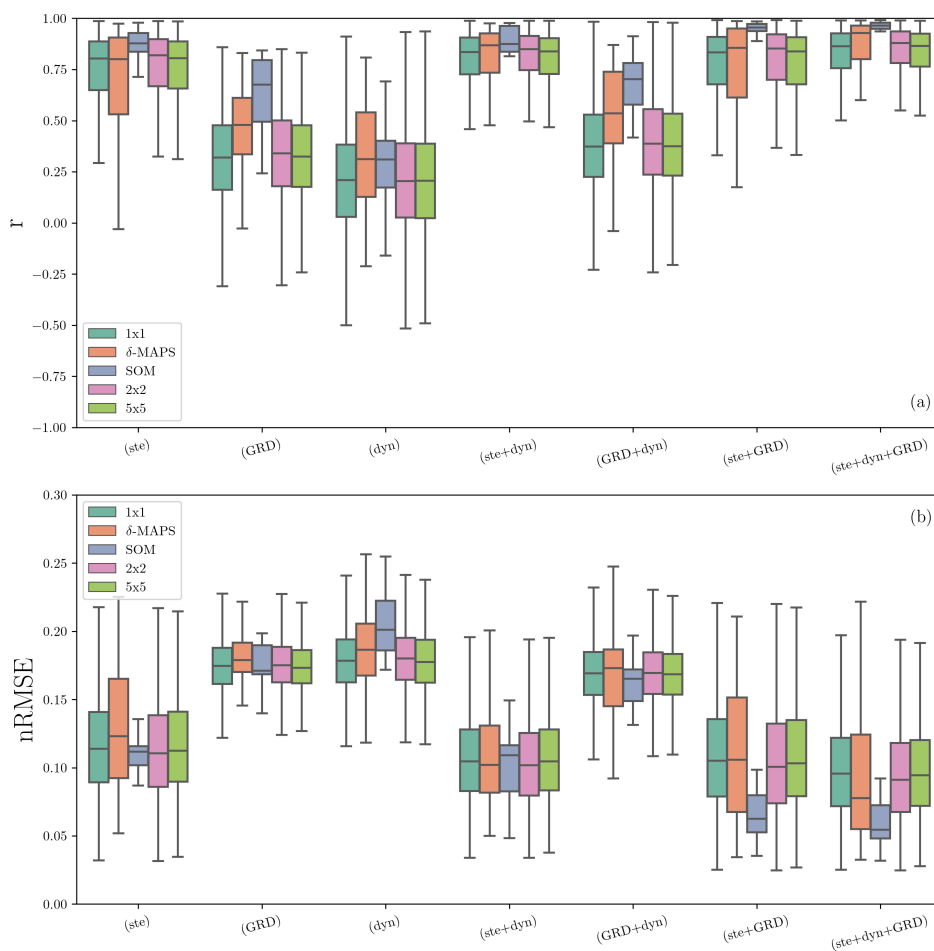
Figure B5. Same as Figure 5, but including SLB considering blocks of 2x2 and 5x5 degrees. There is no clear improvement from the 1x1 degree budget to the 2x2 and 5x5, showing the added value of using the δ-MAPS and SOM domains.
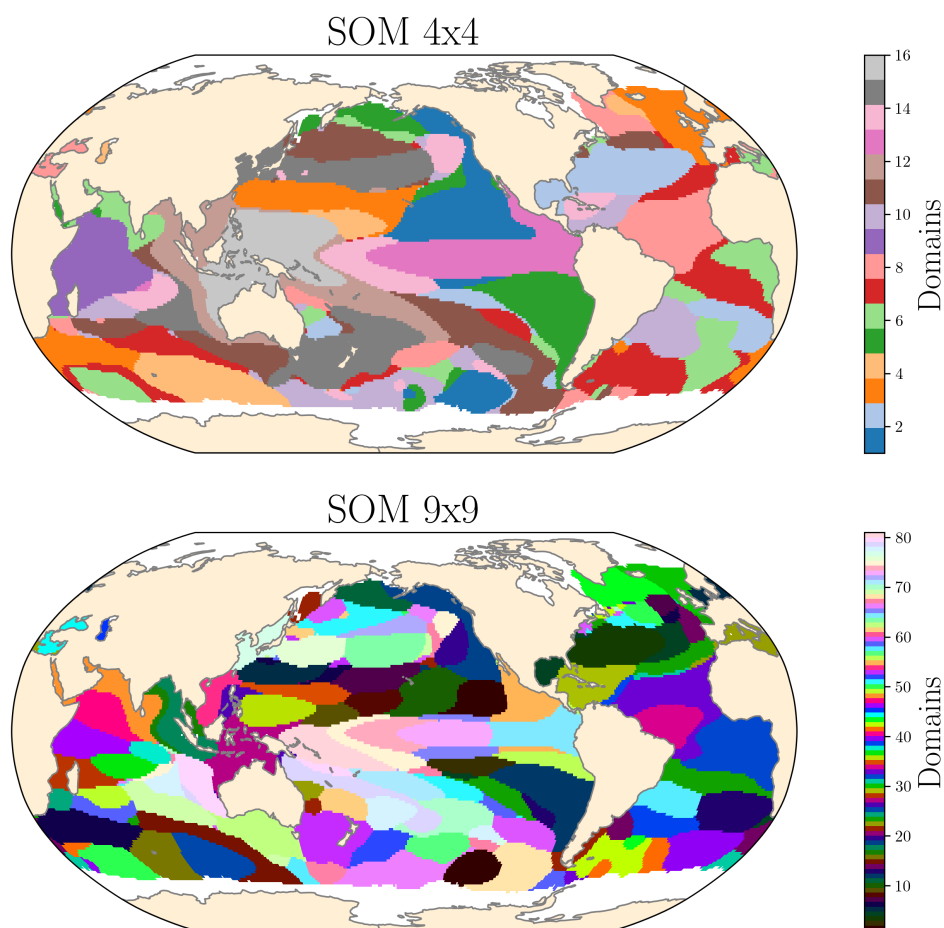
Figure B6. SOM domains for a neural map of (a) 4x4 (a) and of (b) 9x9, using the entire ocean as input for the clustering. Note that, even with a larger neural map, the SOM patterns are still different than the δ-MAPS domains (Figure 2), proving that the difference between the extracted patterns are not just a function of the number of SOM neurons, but due to differences between the two methods. It does, however, leads to less regions that are geographically distant being clustered in the same domain.

Author contributions. CC performed the research and drafted the article. CC, RR and AS designed the study. Self-organising maps methods and analysis were applied by CC, IH-C and MM. CC and ES performed δ-MAPS analysis. All authors contributed to the interpretation of the results and the writing of the manuscript.

Competing interests. The authors declare no competing interests.

Acknowledgements. This research was funded by the Netherlands Space Office User Support program (grant no. ALWGO.2017.002).

References

Akaike, H.: A New Look at the Statistical Model Identification, IEEE Transactions on Automatic Control, 19, 716–723, https://doi.org/10.1109/TAC.1974.1100705, 1974.

Barnoud, A., Pfeffer, J., Guérou, A., Frery, M. L., Siméon, M., Cazenave, A., Chen, J., Llovel, W., Thierry, V., Legeais, J. F., and Ablain, M.: Contributions of Altimetry and Argo to Non-Closure of the Global Mean Sea Level Budget Since 2016, Geophysical Research Letters, 48, 1–10, https://doi.org/10.1029/2021GL092824, 2021.

Bilbao, R. A. F., Gregory, J. M., and Bouttes, N.: Analysis of the regional pattern of sea level change due to ocean dynamics and density change for 1993–2099 in observations and CMIP5 AOGCMs, Climate Dynamics, 45, 2647–2666, https://doi.org/10.1007/s00382-015-2499-z, 2015.

Blockley, E. W., Martin, M. J., McLaren, A. J., Ryan, A. G., Waters, J., Lea, D. J., Mirouze, I., Peterson, K. A., Sellar, A., and Storkey, D.: Recent development of the Met Office operational ocean forecasting system: An overview and assessment of the new Global FOAM forecasts, Geoscientific Model Development, 7, 2613–2638, https://doi.org/10.5194/gmd-7-2613-2014, 2014.

Bos, M. S., Fernandes, R. M., Williams, S. D., and Bastos, L.: Fast error analysis of continuous GNSS observations with missing data, Journal of Geodesy, 87, 351–360, https://doi.org/10.1007/s00190-012-0605-0, 2013.

Bos, M. S., Williams, S. D., Araújo, I. B., and Bastos, L.: The effect of temporal correlated noise on the sea level rate and acceleration uncertainty, Geophysical Journal International, 196, 1423–1430, https://doi.org/10.1093/gji/ggt481, 2014.

Bracco, A., Falasca, F., Nenes, A., Fountalis, I., and Dovrolis, C.: Advancing climate science with knowledge-discovery through data mining, npj Climate and Atmospheric Science, 1, 1–6, https://doi.org/10.1038/s41612-017-0006-4, 2018.

Cabanes, C., Grouazel, A., Von Schuckmann, K., Hamon, M., Turpin, V., Coatanoan, C., Paris, F., Guinehut, S., Boone, C., Ferry, N., De Boyer Montégut, C., Carval, T., Reverdin, G., Pouliquen, S., and Le Traon, P. Y.: The CORA dataset: Validation and diagnostics of in-situ ocean temperature and salinity measurements, Ocean Science, 9, 1–18, https://doi.org/10.5194/os-9-1-2013, 2013.

Calafat, F. M., Chambers, D. P., and Tsimplis, M. N.: Mechanisms of decadal sea level variability in the eastern North Atlantic and the Mediterranean Sea, Journal of Geophysical Research: Oceans, 117, 1–14, https://doi.org/10.1029/2012JC008285, 2012.

Camargo, C. M., Riva, R. E., Hermans, T. H., and Slangen, A. B.: Exploring Sources of Uncertainty in Steric Sea-Level Change Estimates, Journal of Geophysical Research: Oceans, 125, 1–18, https://doi.org/10.1029/2020JC016551, 2020.

Camargo, C. M. L., Riva, R. E. M., Hermans, T. H. J., and Slangen, A. B. A.: ESDD - Trends and Uncertainties of Regional Barystatic Sea-level Change in the Satellite Altimetry Era, Earth Syst. Dynam. Discuss., [preprint], 1–33, https://esd.copernicus.org/preprints/esd-2021-80/, 2021.

Carton, J. A., Chepurin, G. A., and Cheng, L.: SODA3: a new ocean climate reanalysis, Monthly Weather Review, 2018.

Cazenave, A. and Moreira, L.: Contemporary sea-level changes from global to local scales: a review, Proceedings of the Royal Society A: Mathematical, Physical and Engineering Sciences, 478, https://doi.org/10.1098/rspa.2022.0049, 2022.

Cazenave, A., Meyssignac, B., Ablain, M., Balmaseda, M., Bamber, J., Barletta, V., Beckley, B., Benveniste, J., Berthier, E., Blazquez, A., Boyer, T., Caceres, D., Chambers, D., Champollion, N., Chao, B., Chen, J., Cheng, L., Church, J. A., Chuter, S., Cogley, J. G., Dangendorf, S., Desbruyères, D., Döll, P., Domingues, C., Falk, U., Famiglietti, J., Fenoglio-Marc, L., Forsberg, R., Galassi, G., Gardner, A., Groh, A., Hamlington, B., Hogg, A., Horwath, M., Humphrey, V., Husson, L., Ishii, M., Jaeggi, A., Jevrejeva, S., Johnson, G., Kolodziejczyk, N., Kusche, J., Lambeck, K., Landerer, F., Leclercq, P., Legresy, B., Leuliette, E., Llovel, W., Longuevergne, L., Loomis, B. D., Luthcke, S. B., Marcos, M., Marzeion, B., Merchant, C., Merrifield, M., Milne, G., Mitchum, G., Mohajerani, Y., Monier, M., Monselesan, D.,

455   Nerem, S., Palanisamy, H., Paul, F., Perez, B., Piecuch, C. G., Ponte, R. M., Purkey, S. G., Reager, J. T., Rietbroek, R., Rignot, E., Riva,
R., Roemmich, D. H., Sørensen, L. S., Sasgen, I., Schrama, E. J., Seneviratne, S. I., Shum, C. K., Spada, G., Stammer, D., van de Wal, R.,
Velicogna, I., von Schuckmann, K., Wada, Y., Wang, Y., Watson, C., Wiese, D., Wijffels, S., Westaway, R., Woppelmann, G., and Wouters,
B.: Global sea-level budget 1993-present, Earth System Science Data, 10, 1551–1590, https://doi.org/10.5194/essd-10-1551-2018, 2018.

Chafik, L., Nilsen, J. E. Ø., Dangendorf, S., Reverdin, G., and Frederikse, T.: North Atlantic Ocean Circulation and Decadal Sea Level
460   Change During the Altimetry Era, Scientific Reports, 9, 1–9, https://doi.org/10.1038/s41598-018-37603-6, 2019.

Chambers, D. P., Wahr, J., and Nerem, R. S.: Preliminary observations of global ocean mass variations with GRACE, Geophysical Research
Letters, 31, 1–4, https://doi.org/10.1029/2004GL020461, 2004.

Chen, J., Tapley, B., Wilson, C., Cazenave, A., Seo, K. W., and Kim, J. S.: Global Ocean Mass Change From GRACE and GRACE Follow-On
and Altimeter and Argo Measurements, Geophysical Research Letters, 47, 1–9, https://doi.org/10.1029/2020GL090656, 2020.

465   Chen, J. L., Wilson, C. R., Tapley, B. D., and Grand, S.: GRACE detects coseismic and postseismic deformation from the Sumatra-Andaman
earthquake, Geophysical Research Letters, 34, 1–5, https://doi.org/10.1029/2007GL030356, 2007.

Cheng, L., Abraham, J., Hausfather, Z., and Trenberth, K. E.: How fast are the oceans warming ?, Science Climate Change, 128, 1–8,
https://doi.org/10.1126/science.aav7619, 2019.

CMEMS: GLOBAL OCEAN GRIDDED L4 SEA SURFACE HEIGHTS AND DERIVED VARIABLES REPROCESSED (1993-
470   ONGOING) SEALEVEL_GLO_PHY_L4_MY_008_047, https://doi.org/https://doi.org/10.48670/moi-00148, 2022.

CSIRO: Combined TOPEX Poseidon, Jason-1, Jason-2 OSTM, Jason-3 near-global gridded monthly-average sea level product.,
https://doi.org/http://www.cmar.csiro.au/sealevel/sl_data_cmar.html, 2022.

Dangendorf, S., Frederikse, T., Chafik, L., Klinck, J. M., Ezer, T., and Hamlington, B. D.: Data-driven reconstruction reveals large-scale
ocean circulation control on coastal sea level, Nature Climate Change, 11, 514–520, https://doi.org/10.1038/s41558-021-01046-1, 2021.

475   Falasca, F., Bracco, A., Nenes, A., and Fountalis, I.: Dimensionality Reduction and Network Inference for Climate Data Using δ-MAPS:
Application to the CESM Large Ensemble Sea Surface Temperature, Journal of Advances in Modeling Earth Systems, 11, 1479–1515,
https://doi.org/10.1029/2019MS001654, 2019.

Falasca, F., Crétat, J., Braconnot, P., and Bracco, A.: Spatiotemporal complexity and time-dependent networks in sea surface temperature
from mid- to late Holocene, European Physical Journal Plus, 135, 1–21, https://doi.org/10.1140/epjp/s13360-020-00403-x, 2020.

480   Farrell, W. E. and Clark, J. A.: On Postglacial Sea Level, Geophysical Journal of the Royal Astronomical Society, 46, 647–667, 1976.

Feng, M., Li, Y., and Meyers, G.: Multidecadal variations of Fremantle sea level: Footprint of climate variability in the tropical Pacific,
Geophysical Research Letters, 31, 2–5, https://doi.org/10.1029/2004GL019947, 2004.

Fountalis, I., Dovrolis, C., Bracco, A., Dilkina, B., and Keilholz, S.: δ-MAPS: from spatio-temporal data to a weighted and lagged network
between functional domains, Applied Network Science, 3, https://doi.org/10.1007/s41109-018-0078-z, 2018.

485   Fox-Kemper, B., Hewitt, H., Xiao, C., Aðalgeirsdóttir, G., Drijfhout, S., Edwards, T., Golledge, N., Hemer, M., Kopp, R., Krinner, G., Mix,
A., Notz, D., Nowicki, S., Nurhati, I., Ruiz, L., Sallée, J.-B., Slangen, A., and Yu, Y.: Ocean, Cryosphere and Sea Level Change, in: Climate
Change 2021: The Physical Science Basis. Contribution of Working Group I to the Sixth Assessment Report of the Intergovernmental
Panel on Climate Change, edited by MassonDelmotte, V., Zhai, P., Pirani, A., Connors, S., Péan, C., Berger, S., Caud, N., Chen, Y.,
Goldfarb, L., Gomis, M., Huang, M., Leitzell, K., Lonnoy, E., Matthews, J., Maycock, T., Waterfield, T., Yelekçi, O., Yu, R., and Zhou,
490   B., vol. In Press, chap. 9, p. 73, Cambridge University Press, 2021.

Frederikse, T., Jevrejeva, S., Riva, R. E., and Dangendorf, S.: A consistent sea-level reconstruction and its budget on basin and global scales
over 1958-2014, Journal of Climate, 31, 1267–1280, https://doi.org/10.1175/JCLI-D-17-0502.1, 2018.

Frederikse, T., Landerer, F., Caron, L., Adhikari, S., Parkes, D., Humphrey, V. W., Dangendorf, S., Hogarth, P., Zanna, L., and Cheng, L.: The causes of sea-level rise since 1900, Nature, 584, https://doi.org/10.1038/s41586-020-2591-3, 2020.

495 Gaillard, F., Reynaud, T., Thierry, V., Kolodziejczyk, N., and Von Schuckmann, K.: In situ-based reanalysis of the global ocean temperature and salinity with ISAS: Variability of the heat content and steric height, Journal of Climate, 29, 1305–1323, https://doi.org/10.1175/JCLI-D-15-0028.1, 2016.

Garric, G. and Parent, L.: Quality Information Document For products GLOBAL-REANALYSIS-PHY-001-025, Tech. rep., Copernicus Marine Environment Monitoring Service, 2017.

500 Ghobadi-Far, K., Han, S. C., Allgeyer, S., Tregoning, P., Sauber, J., Behzadpour, S., Mayer-Gürr, T., Sneeuw, N., and Okal, E.: GRACE gravitational measurements of tsunamis after the 2004, 2010, and 2011 great earthquakes, Journal of Geodesy, 94, 1–9, https://doi.org/10.1007/s00190-020-01395-3, 2020.

Gill, A. E. and Niller, P. P.: The theory of the seasonal variability in the ocean, Deep Sea Research and Oceanographic Abstracts, 20, 141–177, https://doi.org/https://doi.org/10.1016/0011-7471(73)90049-1, 1973.

505 Good, S. A., Martin, M. J., and Rayner, N. A.: EN4: Quality controlled ocean temperature and salinity profiles and monthly objective analyses with uncertainty estimates, Journal of Geophysical Research: Oceans, 118, 6704–6716, https://doi.org/10.1002/2013JC009067, 2013.

Gregory, J. M., White, N. J., Church, J. A., Bierkens, M. F., Box, J. E., Van Den Broeke, M. R., Cogley, J. G., Fettweis, X., Hanna, E., Huybrechts, P., Konikow, L. F., Leclercq, P. W., Marzeion, B., Oerlemans, J., Tamisiea, M. E., Wada, Y., Wake, L. M., and Van De Wal, R. S.: Twentieth-century global-mean sea level rise: Is the whole greater than the sum of the parts?, Journal of Climate, 26, 4476–4499,
510 https://doi.org/10.1175/JCLI-D-12-00319.1, 2013.

Gregory, J. M., Griffies, S. M., Hughes, C. W., Lowe, J. A., Church, J. A., Fukimori, I., Gomez, N., Kopp, R. E., Landerer, F., Cozannet, G. L., Ponte, R. M., Stammer, D., Tamisiea, M. E., and van de Wal, R. S.: Concepts and Terminology for Sea Level: Mean, Variability and Change, Both Local and Global, Surveys in Geophysics, 40, 1251–1289, https://doi.org/10.1007/s10712-019-09525-z, 2019.

Griffies, S. M. and Greatbatch, R. J.: Physical processes that impact the evolution of global mean sea level in ocean climate models, Ocean
515 Modelling, 51, 37–72, https://doi.org/10.1016/j.ocemod.2012.04.003, 2012.

Guinehut, S., Dhomps, A. L., Larnicol, G., and Le Traon, P. Y.: High resolution 3-D temperature and salinity fields derived from in situ and satellite observations, Ocean Science, 8, 845–857, https://doi.org/10.5194/os-8-845-2012, 2012.

Hamlington, B. D., Gardner, A. S., Ivins, E., Lenaerts, J. T., Reager, J. T., Trossman, D. S., Zaron, E. D., Adhikari, S., Arendt, A., Aschwanden, A., Beckley, B. D., Bekaert, D. P., Blewitt, G., Caron, L., Chambers, D. P., Chandanpurkar, H. A., Christianson, K., Csatho,
520 B., Cullather, R. I., DeConto, R. M., Fasullo, J. T., Frederikse, T., Freymueller, J. T., Gilford, D. M., Girotto, M., Hammond, W. C., Hock, R., Holschuh, N., Kopp, R. E., Landerer, F., Larour, E., Menemenlis, D., Merrifield, M., Mitrovica, J. X., Nerem, R. S., Nias, I. J., Nieves, V., Nowicki, S., Pangaluru, K., Piecuch, C. G., Ray, R. D., Rounce, D. R., Schlegel, N. J., Seroussi, H., Shirzaei, M., Sweet, W. V., Velicogna, I., Vinogradova, N., Wahl, T., Wiese, D. N., and Willis, M. J.: Understanding of Contemporary Regional Sea-Level Change and the Implications for the Future, Reviews of Geophysics, 58, 1–39, https://doi.org/10.1029/2019RG000672, 2020.

525 Han, W., Meehl, G. A., Stammer, D., Hu, A., Hamlington, B., Kenigson, J., Palanisamy, H., and Thompson, P.: Spatial Patterns of Sea Level Variability Associated with Natural Internal Climate Modes, Surveys in Geophysics, 38, 217–250, https://doi.org/10.1007/s10712-016-9386-y, 2017.

Hermans, T. H., Le Bars, D., Katsman, C. A., Camargo, C. M., Gerkema, T., Calafat, F. M., Tinker, J., and Slangen, A. B.: Drivers of Interannual Sea Level Variability on the Northwestern European Shelf, Journal of Geophysical Research: Oceans, 125, 1–18,
530 https://doi.org/10.1029/2020JC016325, 2020.

Hernández-Carrasco, I. and Orfila, A.: The Role of an Intense Front on the Connectivity of the Western Mediterranean Sea: The Cartagena-Tenes Front, Journal of Geophysical Research: Oceans, 123, 4398–4422, https://doi.org/10.1029/2017JC013613, 2018.

Hughes, C. W. and Williams, S. D.: The color of sea level: Importance of spatial variations in spectral shape for assessing the significance of trends, Journal of Geophysical Research: Oceans, 115, https://doi.org/10.1029/2010JC006102, 2010.

535 Hughes, C. W., Fukumori, I., Griffies, S. M., Huthnance, J. M., Minobe, S., Spence, P., Thompson, K. R., and Wise, A.: Sea Level and the Role of Coastal Trapped Waves in Mediating the Influence of the Open Ocean on the Coast, Surveys in Geophysics, 40, 1467–1492, https://doi.org/10.1007/s10712-019-09535-x, 2019.

Ishii, M. and Kimoto, M.: Reevaluation of historical ocean heat content variations with time-varying XBT and MBT depth bias corrections, Journal of Oceanography, 65, 287–299, https://doi.org/10.1007/s10872-009-0027-7, 2009.

540 Ishii, M., Yasui, S., Fukuda, Y., Sato, K., Hirahara, S., and Suzuki, T.: Accuracy of Global Upper Ocean Heat Content Estimation Expected from Present Observational Data Sets, Sola, 13, 163–167, https://doi.org/10.2151/sola.2017-030, 2017.

Kleinherenbrink, M., Riva, R., Frederikse, T., Merrifield, M., and Wada, Y.: Trends and interannual variability of mass and steric sea level in the Tropical Asian Seas, Journal of Geophysical Research: Oceans, 122, 6254–6276, https://doi.org/10.1002/2017JC012792, 2017.

Kohonen, T.: Self-organized formation of topologically correct feature maps, Biological Cybernetics, 43, 59–69, 545 https://doi.org/10.1007/BF00337288, 1982.

Landerer, F. W., Jungclaus, J. H., and Marotzke, J.: Ocean bottom pressure changes lead to a decreasing length-of-day in a warming climate, Geophys. Res. Lett., 34, http://dx.doi.org/10.1029/2006GL029106, 2007.

Li, H., Xu, F., Zhou, W., Wang, D., Wright, J. S., Liu, Z., and Lin, Y.: Development of a global gridded Argo data set with Barnes successive corrections, Journal of Geophysical Research: Oceans, 122, 866–889, https://doi.org/10.1002/2016JC012285, 2017.

550 Liu, Y., Weisberg, R. H., and Mooers, C. N.: Performance evaluation of the self-organizing map for feature extraction, Journal of Geophysical Research: Oceans, 111, 1–14, https://doi.org/10.1029/2005JC003117, 2006.

Liu, Y., Weisberg, R. H., Vignudelli, S., and Mitchum, G. T.: Patterns of the loop current system and regions of sea surface height variability in the eastern Gulf of Mexico revealed by the self-organizing maps, Journal of Geophysical Research: Oceans, 121, 2347–2366, https://doi.org/10.1002/2015JC011493.Received, 2016.

555 Lu, S., Liu, Z., Li, H., Li, Z., Wu, X., and Sun, C.: Manual of Global Ocean Argo gridded data set (BOA_Argo) (Version 2019), Tech. rep., Second Institue of oceanography SOA, https://doi.org/10.1002/2016JC012285.6, 2019.

MA, F., DIAO, Y. N., and LUO, D. H.: Spatiotemporal characteristics of the sea level anomaly in the Kuroshio Extension using a self-organizing map, Atmospheric and Oceanic Science Letters, 9, 471–478, https://doi.org/10.1080/16742834.2016.1235462, 2016.

MacIntosh, C. R., Merchant, C. J., and von Schuckmann, K.: Uncertainties in Steric Sea Level Change Estimation During the Satellite 560 Altimeter Era: Concepts and Practices, Surveys in Geophysics, 38, 59–87, https://doi.org/10.1007/s10712-016-9387-x, 2017.

Maclachlan, C., Arribas, A., Peterson, K. A., Maidens, A., Fereday, D., Scaife, A. A., Gordon, M., Vellinga, M., Williams, A., Comer, R. E., Camp, J., Xavier, P., Madec, G., and National, F.: Global Seasonal forecast system version 5 (GloSea5): a high-resolution seasonal forecast system, Quarterly Journal of the Royal Meteorological Society, 5, 1072–1084, https://doi.org/10.1002/qj.2396, 2015.

Marcos, M. and Amores, A.: Geophysical Research Letters, Geophysical Research Letters, 41, 2502–2507, 565 https://doi.org/10.1002/2014GL059766.Received, 2014.

Novi, L., Bracco, A., and Falasca, F.: Uncovering marine connectivity through sea surface temperature, Scientific Reports, 11, 1–9, https://doi.org/10.1038/s41598-021-87711-z, 2021.

Pattiaratchi, C. and Siji, P.: Variability in ocean currents around Australia, in: State and Trends of Australia's Ocean Report, edited by Richardson, A., Eriksen, R., Moltmann, T., Hodgson-Johnston, I., and Wallis, J., January 2020, chap. 1.4 Variab, pp. 1–6, Integrated Marine Observing System (IMOS), https://doi.org/10.26198/5e16a2ae49e76, 2020.

Purkey, S. G. and Johnson, G. C.: Warming of Global Abyssal and Deep Southern Ocean Waters between the 1990s and 2000s: Contributions to Global Heat and Sea Level Rise Budgets, Journal of Climate, 23, 6336–6351, https://doi.org/10.1175/2010JCLI3682.1, 2010.

Purkey, S. G., Johnson, G. C., and Chambers, D. P.: Sea contributions of ocean mass and deep steric changes to sea level rise between 1993 and 2013, Journal of Geophysical Research : Oceans, 119, 7509–7522, https://doi.org/10.1002/2014JC010180, 2014.

Purkey, S. G., Johnson, G. C., Talley, L. D., Sloyan, B. M., Wijffels, S. E., Smethie, W., Mecking, S., and Katsumata, K.: Unabated Bottom Water Warming and Freshening in the South Pacific Ocean, Journal of Geophysical Research: Oceans, 124, 1778–1794, https://doi.org/10.1029/2018JC014775, 2019.

Richardson, A. J., Risi En, C., and Shillington, F. A.: Using self-organizing maps to identify patterns in satellite imagery, Progress in Oceanography, 59, 223–239, https://doi.org/10.1016/j.pocean.2003.07.006, 2003.

Rietbroek, R., Brunnabend, S.-E., Kusche, J., Schröter, J., and Dahle, C.: Revisiting the contemporary sea-level budget on global and regional scales, Proceedings of the National Academy of Sciences, 113, 1504–1509, https://doi.org/10.1073/pnas.1519132113, 2016.

Roemmich, D. and Gilson, J.: The 2004 – 2008 mean and annual cycle of temperature , salinity , and steric height in the global ocean from the Argo Program, Progress in Oceanography, 82, 81–100, https://doi.org/10.1016/j.pocean.2009.03.004, 2009.

Rougier, J.: Ensemble averaging and mean squared error, Journal of Climate, 29, 8865–8870, https://doi.org/10.1175/JCLI-D-16-0012.1, 2016.

Royston, S., Watson, C. S., Legresy, B., King, M. A., Church, J. A., and Bos, M. S.: Sea-Level Trend Uncertainty With Pacific Climatic Variability and Temporally-Correlated Noise, Journal of Geophysical Research : Oceans2, 123, 1978–1993, 2018.

Royston, S., Vishwakarma, B. D., Westaway, R., Rougier, J., Sha, Z., and Bamber, J.: Can We Resolve the Basin-Scale Sea Level Trend Budget From GRACE Ocean Mass?, Journal of Geophysical Research: Oceans, 125, 1–16, https://doi.org/10.1029/2019JC015535, 2020.

Save, H.: CSR GRACE and GRACE-FO RL06 Mascon Solutions v02, CSR, https://doi.org/doi: 10.15781/cgq9-nh24, 2020.

Save, H., Bettadpur, S., and Tapley, B. D.: High-resolution CSR GRACE RL05 mascons, Journal of Geophysical Research : Solid Earth, 121, 7547–7569, https://doi.org/10.1002/2017JB015312, 2016.

Schwarz, G.: Estimating the dimension of a model, Annals of Statistics, 6, 461–464, https://doi.org/10.1214/aos/1176344136, 1978.

Slangen, A. B., Van De Wal, R. S., Wada, Y., and Vermeersen, L. L.: Comparing tide gauge observations to regional patterns of sea-level change (1961-2003), Earth System Dynamics, 5, 243–255, https://doi.org/10.5194/esd-5-243-2014, 2014.

Slangen, A. B., Church, J. A., Agosta, C., Fettweis, X., Marzeion, B., and Richter, K.: Anthropogenic forcing dominates global mean sea-level rise since 1970, Nature Climate Change, 6, 701–705, https://doi.org/10.1038/nclimate2991, 2016.

Slangen, A. B. A., Adloff, F., Jevrejeva, S., Leclercq, P. W., Marzeion, B., Wada, Y., and Winkelmann, R.: A Review of Recent Updates of Sea-Level Projections at Global and Regional Scales, Surveys in Geophysics, 38, 385–406, https://doi.org/10.1007/s10712-016-9374-2, 2017.

SLcci, E.: Time series of gridded sea level anomalies, https://doi.org/10.5270/esa-sea, 2022.

Sonnewald, M., Wunsch, C., and Heimbach, P.: Linear predictability: A sea surface height case study, Journal of Climate, 31, 2599–2611, https://doi.org/10.1175/JCLI-D-17-0142.1, 2018.

Sonnewald, M., Wunsch, C., and Heimbach, P.: Unsupervised Learning Reveals Geography of Global Ocean Dynamical Regions, Earth and Space Science, 6, 784–794, https://doi.org/10.1029/2018EA000519, 2019.

Stammer, D., Cazenave, A., Ponte, R. M., and Tamisiea, M. E.: Causes for Contemporary Regional Sea Level Changes, Annu Rev Marine Sci, 5, https://doi.org/10.1146/annurev-marine-121211-172406, 2013.

Storto, A. and Masina, S.: C-GLORSv5: An improved multipurpose global ocean eddy-permitting physical reanalysis, Earth System Science Data, 8, 679–696, https://doi.org/10.5194/essd-8-679-2016, 2016.

610   Storto, A., Masina, S., Balmaseda, M., Guinehut, S., Xue, Y., Szekely, T., Fukumori, I., Forget, G., Chang, Y. S., Good, S. A., Köhl, A., Vernieres, G., Ferry, N., Peterson, K. A., Behringer, D., Ishii, M., Masuda, S., Fujii, Y., Toyoda, T., Yin, Y., Valdivieso, M., Barnier, B., Boyer, T., Lee, T., Gourrion, J., Wang, O., Heimback, P., Rosati, A., Kovach, R., Hernandez, F., Martin, M. J., Kamachi, M., Kuragano, T., Mogensen, K., Alves, O., Haines, K., and Wang, X.: Steric sea level variability (1993–2010) in an ensemble of ocean reanalyses and objective analyses, Climate Dynamics, 49, 709–729, https://doi.org/10.1007/s00382-015-2554-9, 2017.

615   Szekely, T., Gourrion, J., Pouliquen, S., and Reverdin, G.: The CORA 5.2 dataset for global in situ temperature and salinity measurements: Data description and validation, Ocean Science, 15, 1601–1614, https://doi.org/10.5194/os-15-1601-2019, 2019.

Tapley, B. D., Bettadpur, S., Watkins, M., and Reigber, C.: The Gravity Recovery and Climate Experiment: Mission Overview and Early Results, Geophysical Research Letters, 31, 1–4, https://doi.org/10.1029/2004GL019920, 2004.

Thompson, P. R. and Merrifield, M. A.: A unique asymmetry in the pattern of recent sea level change, Geophysical Research Letters, 41, 620   7675–7683, https://doi.org/10.1002/2014GL061263, 2014.

Vesanto, J., HImberg, J., Alhoniemi, E., and Parhankangaas, J.: SOM Toolbox for Matlab 5, Tech. rep., Helsinki University of Technology, 2000.

Wagner, P. and Böning, C. W.: Decadal sea-level variability in the Australasian Mediterranean Sea, Ocean Science, 17, 1473–1487, https://doi.org/10.5194/os-17-1473-2021, 2021.

625   Wang, J., Church, J. A., Zhang, X., Gregory, J. M., Zanna, L., and Chen, X.: Evaluation of the Local Sea-Level Budget at Tide Gauges Since 1958, Geophysical Research Letters, 48, 1–12, https://doi.org/10.1029/2021GL094502, 2021.

Watkins, M. M., Wiese, D. N., Yuan, D.-N., Boening, C., and Landerer, F. W.: Improved methods for observing Earth's time variable mass distribution with GRACE using spherical cap mascons, JGR: Solid Earth, 120, 1648–2671, https://doi.org/10.1002/2014JB011547, 2015.

Wiese, D. N., Yuan, D.-N., Boening, C., Landerer, F. W., and M., W. M.:   JPL GRACE Mascon Ocean, Ice, and Hydrology 630   Equivalent Water Height RL06 CRI Filtered Version 02. Ver. 02. PO.DAAC, CA, USA., JPL, Dataset accessed [2020-10-28], https://doi.org/https://doi.org/10.5067/TEMSC-3JC62, 2019.

Wöppelmann, G. and Marcos, M.: Vertical land motion as a key to understanding sea level change and variability, Reviews of Geophysics, 54, 64–92, https://doi.org/10.1002/2015RG000502.Received, 2015.

Zlotnicki, V., Qu, Z., Willis, J. K., Ray, R., and Hausman, J.: JPL MEASURES Gridded Sea Surface Height Anomalies Version JPL1812, 635   https://doi.org/doi.org/10.5067/SLREF-CDRV2, 2019.

Zuo, H., Balmaseda, M. A., Tietsche, S., Mogensen, K., and Mayer, M.: The ECMWF operational ensemble reanalysis-analysis system for ocean and sea ice: A description of the system and assessment, Ocean Science, 15, 779–808, https://doi.org/10.5194/os-15-779-2019, 2019.